RIS-Based Dual-Mode Receive Spatial Modulation for Low-Complexity Wireless Access Points

Tufail Ahmad, *Student Member, IEEE*, and Ertugrul Basar, *Fellow, IEEE*

***Abstract*—The emerging technology of reconfigurable intelligent surface-based access points (RIS-APs) shows excellent potential as it effectively replaces conventional RF front ends with passive RISs. This paper introduces RIS-based dual-mode receive spatial modulation (RDM-RSM), a low-complexity scheme designed to improve the spectral efficiency and error performance of RIS-APs. Both versions of the proposed RDM-RSM scheme configure the RIS to simultaneously enhance the RF signals at two different receive antennas while synthesizing distinct modulation symbols from two separate constellations at each antenna, thereby enabling efficient transmission of two parallel, conventionally-modulated data-streams. Additionally, by selecting two antennas and assigning each a distinct constellation mode, more bits can be encoded per index-modulated symbol. The first version, RDM-RSM-Independent (RDM-RSMI), operates by maximizing the energy of the synthesized signals *independently* for each antenna. In contrast, RDM-RSM-Joint (RDM-RSMJ) optimizes the reflection phase of each RIS element to maximize an objective function that considers the signals at both antennas *jointly*, resulting in stronger received signals compared to RDM-RSMI, where only half of the elements can serve each antenna. A low-complexity detector is proposed, with its theoretical performance rigorously analyzed by modeling the conditional reflection phases of the RIS elements as von-Mises distributed, providing a tractable and insightful framework.**

***Index Terms*—Reconfigurable intelligent surface (RIS), index modulation (IM), receive spatial modulation (RSM).**

I. Introduction

WIRELESS communication systems have evolved over time primarily in response to the growing demand for higher data rates. However, with the densification of networks and the increasing number of users, additional considerations such as low-complexity, cost-effectiveness, and improved energy and spectral efficiencies have become crucial in the design of modern wireless systems. To address these challenges, emerging technologies like index modulation (IM) and reconfigurable intelligent surfaces (RISs) have garnered significant attention due to their ability to reduce energy consumption, minimize costs and complexity, and improve the overall performance of wireless networks.

IM is an innovative, unconventional modulation approach that conveys information through the indices of a communication network's resource rather than modulating a signal with a conventional constellation symbol [1]. For example, spatial modulation (SM) encodes information using the indices of activated antennas in a multiple-antenna system [2]. Transmit SM (TSM) and receive SM (RSM) employ the indices of transmit and receive antennas, respectively, for IM [3].

RIS is a transformative addition to the physical layer of wireless systems, enabling active configuration of the wireless channel [4]. Composed of a grid of small, passive, low-cost reflecting elements, an RIS can reflect incident signals with adjustable phase shifts. RIS's ability to dynamically control the channel in a programmable manner makes it well-suited for designing efficient RIS-based IM schemes that can enable low-complexity wireless data transmission [5], [6], [7], [8], [9], [10], [11].

Recently, RIS has emerged as an active research area in academia and industry, owing to its versatility and broad range of potential applications. Beyond modulation—which is the primary focus of this paper—RIS has been explored across several other domains, including enhanced wireless connectivity, coverage extension, sensing, and security [12], [13], [14], [15]. To highlight a few notable use cases for interested readers: RIS has been widely studied for massive IoTs connectivity, Industry 4.0, and future cellular systems including 6G and beyond [16], [17], [18], as well as for vehicular and ground-to-air communications under blockage conditions [19], [20]. Additionally, RIS has shown promise in localization and integrated sensing and communication (ISAC) systems [21], [22]. In physical-layer security, RIS has been utilized to create artificial nulls, helping secure confidential transmissions [23], [24].

A. Motivation and Related Works

This work is primarily motivated by the need for low-complexity and spectrally-efficient wireless APs. A promising solution in this context is the RIS-based access points (RIS-APs), which reduce the complexity by utilizing a passive RIS for modulation, channel co-phasing, and beamforming, requiring an unmodulated RF source as the only active component, unlike the traditional APs that rely on complex transmitter blocks and RF front ends for these communication tasks [9]. The AP design is simplified due to the passive and

Received 9 January 2025; revised 17 May 2025, 26 August 2025, and 22 October 2025; accepted 23 October 2025. Date of publication 4 November 2025; date of current version 22 December 2025. This work was supported in part by TUBITAK 2244 Project under Grant 119C157 and in part by Vestel Electronics. The associate editor coordinating the review of this article and approving it for publication was C.-K. Wen. *(Corresponding author: Ertugrul Basar.)*

Tufail Ahmad is with the Communications Research and Innovation Laboratory (CoreLab), Koç University, Sariyer, 34450 Istanbul, Türkiye (e-mail: tahmad20@ku.edu.tr).

Ertugrul Basar is with the Department of Electrical Engineering, Tampere University, 33720 Tampere, Finland, on leave from the Department of Electrical and Electronics Engineering, Koç University, Sariyer, 34450 Istanbul, Türkiye (e-mail: ebasar@ku.edu.tr).

Digital Object Identifier 10.1109/TWC.2025.3625994

© 2025 The Authors. This work is licensed under a Creative Commons Attribution 4.0 License.
For more information, see https://creativecommons.org/licenses/by/4.0/

comprehensive operation of the RIS; however, this also limits the AP's spectral efficiency (SE) since data can be transmitted only using phase and index modulation. In this regard, several modulation schemes have been proposed; however, they either suffer from limited SE or exhibit poor error performance.

The introduction of RIS-SSK in [9] marks a pioneering step toward RIS-based IM schemes. This innovative scheme leverages an RIS to steer and enhance the reflected signal at one of the receive antennas, with data encoded in the indices of these antennas. RIS-RQRM [10] further improves its SE by reflecting signals in two orthogonal modes—directing the real and imaginary components of the signal to two receive antennas. It partitions the RIS so that each half independently steers the signal to one of the antennas. RIS-RQSSK [25] improves the error performance of RIS-RQRM by using all elements to amplify both components of the reflected signal. RIS-SM in [9] combines conventional modulation with IM to improve the SE of RIS-SSK, i.e., the reflected signal toward the selected receive antenna is also phase-modulated.

The RIS-RQSM scheme in [8] transmits a QAM symbol's real and imaginary components to two antennas independently, thereby enhancing SE. However, this scheme requires additional hardware to dynamically adjust the RF signal power according to the QAM symbol and a one-tap zero-forcing (ZF) pre-equalizer at the transmitter side. Recently, the authors who introduced RIS-RQSM and RIS-RQSSK also proposed RIS-GRQSM [26], which improves the SE of RIS-RQSSK by selecting multiple antennas independently for the real and imaginary components of the signal. The LIS-GSM scheme in [27] enhances SE by adjusting both the transmitter RF power and RIS phases for the conventionally modulated data streams while partitioning the RIS for each selected antenna to transmit the IM data stream. Since each antenna is served by only one of the RIS partitions, the signal at each antenna is relatively weaker. Consequently, its performance degrades as SE increases. It is important to note—as will become clear in the next section—that RIS-RQSM, LIS-GSM, and RIS-SM with QAM are not directly compatible with our low-complexity RIS-AP model due to their additional hardware and processing requirements, as discussed above. We include these schemes in our discussion primarily to highlight the novelty of our proposed schemes.

B. Contributions

This paper proposes RIS-based dual-mode receive spatial modulation (RDM-RSM), a low-complexity scheme specifically designed for RIS-APs. RDM-RSM provides both higher SE and improved error performance, outperforming existing related modulation schemes. RDM-RSM works by intelligently configuring the RIS to simultaneously enhance the RF signals at two different receive antennas while synthesizing a modulation symbol chosen from the first constellation at one antenna and a symbol from the second constellation at the other, thereby efficiently transmitting two parallel, conventionally modulated data streams. Additionally, by selecting two antennas and assigning each a distinct constellation mode, the number of antenna permutations is increased, thereby achieving higher SE. Our contributions include:

- We introduce two versions of RDM-RSM. The basic version, RDM-RSM-Independent (RDM-RSMI), operates by maximizing the energy of the synthesized signals *independently* at each of the two selected antennas. RDM-RSMI, though suboptimal in performance, is presented first as it offers insights into the systematic design of the advanced version, RDM-RSM-Joint (RDM-RSMJ).
- RDM-RSMJ, an energy-efficient version of RDM-RSM, works by optimizing the reflection coefficient of each RIS element to maximize an objective function that considers the signals at both antennas *jointly*. Consequently, each and every RIS element serve both antennas simultaneously, significantly improving the SINR at each antenna.
- A two-stage low-complexity (LC) detector is proposed.
- We formulate an approximate closed-form expression for the average bit error probability (ABEP) of RDM-RSM schemes with the proposed LC detector.
- We adopt a novel approach for the theoretical error analysis by modeling the conditional reflection phases of the RIS elements as von Mises distributed. This approach enables a more tractable performance analysis, providing clear insights into system behavior. Furthermore, this analytical framework facilitates the extension of the analysis to the multi-mode version of the RDM-RSM scheme, offering a versatile tool for broader applications.
- Simulations across various scenarios are presented to validate the accuracy of our analytical ABEP expressions.

The remainder of this paper is organized as follows. Section II presents the system model. In Section III, we discuss RDM-RSMI and develop a LC detector. Section IV introduces RDM-RSMJ and provides a comparison with RDM-RSMI. Section V analyzes the theoretical error performance. Section VI presents computer simulations results for comparative analysis. Finally, Section VII concludes the paper.

Notation: Italic lowercase, boldface lowercase, and boldface uppercase letters represent scalars, column vectors, and matrices, respectively. Discrete and finite sets are denoted by uppercase blackboard bold letters. The operations $(.)^{\mathrm{T}}$ and $(.)^{*}$ denote the transpose and complex conjugate, respectively. For a complex number z, $\Re(z)$ and $\Im(z)$ represent the real and imaginary parts, $|z|$ the absolute value, and $\angle z$ the phase angle. For brevity, we may also use $z^{\Re}$ for $\Re(z)$ and $z^{\Im}$ for $\Im(z)$. The floor of a real number z is denoted by $\lfloor z \rfloor$. The binomial coefficient is represented by $\binom{m}{n}$. A circularly symmetric complex Gaussian (CSCG) random variable (RV) z with mean $\mu = \mathbb{E}\{z\}$ and variance $\sigma^2 = \mathbb{V}\{z\}$ is denoted by $z \sim \mathcal{CN}(\mu, \sigma^2)$. The covariance between RVs x and z is represented by $\mathbb{C}\{x, z\}$. The Gaussian Q-function is represented by $Q(.)$, and $j = \sqrt{-1}$.

II. System Model

Fig. 1 illustrates the system model used to demonstrate the proposed RDM-RSM schemes. The employed model uses the concept of the RIS-AP transmission scheme, in which the RIS is an integral part of the transmitter as a modulating unit and reflects the incident RF signal toward the receiver. In this setup, the RF source is the only active component that

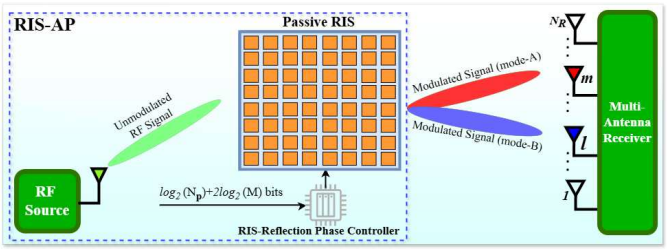


Fig. 1. System model for data transmission using RDM-RSM schemes.

generates an unmodulated RF signal and is equipped with a single antenna to direct the signal toward the RIS. Due to proximity and the line-of-sight (LOS) path between the RIS and the RF source, path loss and fading effects on this link can be ignored. Moreover, it is assumed that the receiver only gets the signal reflected from the RIS. Since the RIS is passive, it utilizes the source-generated RF signal to transmit data by modulating the impinging signal using RDM-RSM. The RIS comprises a total of N reflecting elements, and the phase shifts introduced by each element into the incident RF signal are adjusted electronically by the RIS controller. Both channel equalization (limited to phase equalization) and modulation are performed at the RIS. Subsequently, the signal is reflected toward the receiver, which is equipped with $N_R \geq 2$ antennas. The baseband signal received at antenna $r \in \{1, 2, .., N_R\}$, resulting from the sum of the reflected signals from all RIS elements, is given as below:

$$y_r = \sqrt{E} \sum_{i=1}^{N} h_{r,i} e^{j\theta_{r,i}} \beta_i e^{j\psi_i} + n_r, \tag{1}$$

where E is the energy of the RF signal per transmitted symbol and n_r is the additive white Gaussian noise (AWGN) sample at the r^{th} receive antenna following the distribution $\mathcal{CN}(0, N_0), \forall r$. The channel between the i^{th} RIS element and the r^{th} receive antenna is denoted by $h_{r,i}e^{j\theta_{r,i}}$. Furthermore, all channels are assumed to follow quasi-static block fading [6], and the channel state information (CSI) is available at the RIS. The channel $h_{r,i}e^{j\theta_{r,i}}, \forall (r, i)$ follows the distribution $\mathcal{CN}(0, 1)$, under the assumption of Rayleigh fading.

The complex term $\beta_i e^{j\psi_i}$ in (1) represents the reflection coefficient of the i^{th} RIS element. The reflection amplitude $\beta_i \in [0, 1]$ is set to its maximum value, i.e., $\beta_i = 1, \forall i$, to maximize the power of the RIS-reflected signal. The reflection phase shift, $\psi_i \in [-\pi, \pi)$, can be tuned to phase-equalize the channel associated with the i^{th} RIS element and r^{th} receive antenna. By adjusting $\psi_i = -\theta_{r,i}$ for all RIS elements, the resulting received baseband signal at the r^{th} antenna is given as $y_r = \sqrt{E}\sum_{i=1}^{N} h_{r,i} + n_r$. This leads to boosting the received signal at the r^{th} antenna, and hence data can be encoded in the index $r \in \{1, 2, \ldots, N_R\}$ of the receive antennas to transmit $\lfloor \log_2 N_R \rfloor$ bits. The RIS can further be utilized as a PSK-modulator to transmit additional $\log_2 M$ bits by adjusting $e^{j\psi_i} = e^{j(\phi_A - \theta_{r,i})} = s_A e^{-\theta_{r,i}}$ for all RIS elements, where $s_A = e^{j\phi_A}$ is a modulation symbol selected from the M-PSK constellation $\mathcal{M}_A$. The resulting received baseband signal at the r^{th} antenna is given as $y_r = s_A\sqrt{E}\sum_{i=1}^{N} h_{r,i} + n_r$. With this scheme, the number of bits transmitted per symbol increases to a total of $\log_2 M + \lfloor \log_2 N_R \rfloor$.

The RDM-RSM scheme is designed to further enhance SE, achieving a maximum of $2\log_2 M + \lfloor \log_2 N_R + \log_2(N_R - 1) \rfloor$ bits per channel use (bpcu). To realize this improvement, the proposed design selects two receive antennas at a time, rather than one discussed above. In addition, it employs two distinguishable phase shift keying (PSK) constellations, $\mathcal{M}_A$ and $\mathcal{M}_B$, each of order M and unit energy. For clarity, we explicitly designate the two selected antennas as l and m, where $\mathcal{M}_A$ is used for data transmission to antenna l, and $\mathcal{M}_B$ is used for antenna m. To support this dual-mode transmission, the RDM-RSM scheme methodically configures the RIS to enhance the RF signal power at both antennas l and m simultaneously, while synthesizing a modulation symbol chosen from constellation $\mathcal{M}_A$ at l, and a modulation symbol from $\mathcal{M}_B$ at m. Targeting two antennas at a time and assigning each a distinct constellation mode results in forming a total of $N_R(N_R - 1)$ ordered antenna pairs. In this work, we formally define each such ordered-pair as a permutation $\mathbf{p} = (l, m)$. Consequently, the RDM-RSM scheme can encode up to $\lfloor \log_2 N_R + \log_2(N_R - 1) \rfloor$ IM bits per symbol, compared to $\lfloor \log_2 N_R \rfloor$ bits in the single antenna case discussed above. Moreover, the proposed design enables the efficient transmission of two parallel, conventionally modulated data streams, effectively conveying $2\log_2 M$ data bits compared to only $\log_2 M$ bits in the single antenna case. The constellations $\mathcal{M}_A$ and $\mathcal{M}_B$ can be chosen as any arbitrary, yet distinguishable, PSK constellations. In our system model, we specifically select $\mathcal{M}_B$ as a rotated version of $\mathcal{M}_A$ with a rotation angle of $\frac{\pi}{M}$. This selection is deliberate, as it increases the minimum inter-constellations distance (MIRD), as discussed in [28].

A. Index Mapping for RDM-RSM

We now describe the index mapping method used in this work for the RDM-RSM system, which entails the generation and selection of antenna permutations $\mathbf{p} = (l, m)$, along with the assignment of data bit sequences to these permutations. As discussed above, an RDM-RSM system with N_R receive antennas yields a total of $2\binom{N_R}{2} = N_R(N_R - 1)$ permutations. To transmit p IM bits per symbol, we chose only 2^p permutations, classifying these as the chosen or valid permutations. The remaining permutations are discarded and labeled as invalid, as they are not utilized for data transmission and are therefore not considered during hypothesis testing at the receiver. The cardinality of the chosen/valid permutations for IM is represented as $N_{\mathbf{p}} = 2^p$, where $p \leq \lfloor \log_2 N_R + \log_2(N_R - 1) \rfloor$. Each of these $N_{\mathbf{p}}$ selected permutations is then uniquely mapped to a distinct p-bit data sequence.

As an example, Table I illustrates the modes assigned to antennas l and m for all possible permutations $\mathbf{p} = (l, m)$ in a system with $N_R = 4$. For a given permutation $\mathbf{p}$, we define the set $\mathbb{I}_{\mathbf{p}}$ to represent the indices of the two antennas involved in $\mathbf{p}$, irrespective of the order determined by their assigned modes. Consequently, each index set $\mathbb{I}_{\mathbf{p}}$ corresponds to two associated permutations, which are simply reverse orderings of one another with swapped mode assignments. Thus, the

TABLE I
A LOOKUP TABLE DEMONSTRATING ALL POSSIBLE RECEIVE ANTENNA PERMUTATIONS/ORDERED-PAIRS WITH RDM-RSM FOR $N_R = 4$

#	Permutation $\mathbf{p}=(l,m)$	Antenna Modes	IM bits ($p=3$)
0	$(1,2)$	$\{\mathcal{M}_A^{(1)}, \mathcal{M}_B^{(2)}\}$	[0 0 0]
1	$(1,3)$	$\{\mathcal{M}_A^{(1)}, \mathcal{M}_B^{(3)}\}$	[0 0 1]
2	$(1,4)$	$\{\mathcal{M}_A^{(1)}, \mathcal{M}_B^{(4)}\}$	[0 1 0]
3	$(2,3)$	$\{\mathcal{M}_A^{(2)}, \mathcal{M}_B^{(3)}\}$	[0 1 1]
4	$(2,4)$	$\{\mathcal{M}_A^{(2)}, \mathcal{M}_B^{(4)}\}$	[1 0 0]
5	$(3,4)$	$\{\mathcal{M}_A^{(3)}, \mathcal{M}_B^{(4)}\}$	[1 0 1]
6	$(2,1)$	$\{\mathcal{M}_A^{(2)}, \mathcal{M}_B^{(1)}\}$	[1 1 0]
7	$(3,1)$	$\{\mathcal{M}_A^{(3)}, \mathcal{M}_B^{(1)}\}$	[1 1 1]
8	$(4,1)$	$\{\mathcal{M}_A^{(4)}, \mathcal{M}_B^{(1)}\}$	—
9	$(3,2)$	$\{\mathcal{M}_A^{(3)}, \mathcal{M}_B^{(2)}\}$	—
10	$(4,2)$	$\{\mathcal{M}_A^{(4)}, \mathcal{M}_B^{(2)}\}$	—
11	$(4,3)$	$\{\mathcal{M}_A^{(4)}, \mathcal{M}_B^{(3)}\}$	—

total number of possible index sets $\mathbb{I}_{\mathbf{p}}$ is $\binom{N_R}{2}$, while the total number of distinct permutations $\mathbf{p}$ is $2\binom{N_R}{2}$. Depending on the required number of permutations $N_{\mathbf{p}} = 2^p$, it may be necessary to select both associated permutations for certain index sets $\mathbb{I}_{\mathbf{p}}$, while for others, selecting only one may suffice. For clarity, we define a **reversible permutation** as one whose reverse order counterpart is also included among the chosen permutations for IM. As an illustration, we select the first 8 permutations in Table I to encode $p = 3$ IM bits per symbol. In this scenario, permutation 0 (i.e., $\mathbf{p} = (1,2)$) qualifies as reversible because its reverse, permutation 6 (i.e., $\mathbf{p} = (2,1)$), is also chosen. In contrast, permutation 2 (i.e., $\mathbf{p} = (1,4)$) is not reversible, as its reverse, permutation 8 (i.e., $\mathbf{p} = (4,1)$), is not chosen. This distinction is crucial for the detection process at the receiver and for pairwise error probability (PEP) calculations, which will be discussed in the analysis section.

It is important to note that the index mapping strategy can influence the performance of the RDM-RSM scheme, as is the case with other IM schemes [7], [29]. Although a variety of index mapping strategies can be explored for RDM-RSM, for the sake of clarity and analytical tractability, this work adopts a lookup table-based approach, which is a widely used method in the IM literature [28], [30]. The specific implementation employed in this work is outlined as follows: First, numerical labels ranging from 1 to N_R are assigned to the antennas. Next, all possible antenna permutations (r, r') satisfying $r < r'$, where $r, r' \in \{1, 2, \ldots, N_R\}$, are generated. These resulting $\binom{N_R}{2}$ permutations are then listed in a lexicographical order in the top rows of a table. Subsequently, the corresponding reverse permutations (r', r) of the above sorted original permutations (r, r') are listed in the next $\binom{N_R}{2}$ rows of the table. Numerical labels ranging from 0 to $2\binom{N_R}{2}-1$ are then assigned to these $2\binom{N_R}{2}$ permutations listed in the table. To encode p IM bits per symbol, only the first 2^p permutations are selected, while the rest are discarded. For each selected permutation, the mapped IM bit-sequence corresponds to the p-bit binary representation of its assigned numerical label. As an example, Table I illustrates this index mapping method for an RDM-RSM system with $N_R = 4$ and $p = 3$.

III. WORKING PRINCIPLE OF RDM-RSM SCHEMES AND DESIGN OF A LC DETECTOR

This section explains the design and operation of the RDM-RSMI scheme. Although suboptimal in performance, RDM-RSMI is introduced first as it provides insights into the systematic design of its advanced, energy-efficient version, RDM-RSMJ, which is presented in the next section. Moreover, the signal analysis of the RDM-RSMI scheme facilitates efficient development of a LC detector that applies to both schemes.

A. RDM-RSMI Scheme Design for RIS-AP Systems

The RDM-RSMI scheme configures the reflection phase of each RIS element to enhance the signal exclusively either at antenna l or at antenna m. As a result, the synthesized signals at both antennas in the selected permutation $\mathbf{p} = (l, m)$ are independent of each other. This approach requires that half of the RIS elements serve each antenna to ensure stronger signals at both target antennas. To achieve this, RDM-RSMI partitions the RIS into two halves, with each half dedicated to modulating and enhancing the reflected signal at one of the two selected antennas.

Partition 1: The reflection phase shift of each RIS element in this partition is tuned to match the modulation symbol transmitted to the first antenna in $\mathbf{p}$ (i.e., antenna l), while also performing phase equalization corresponding to the associated channel. Specifically, for the i^{th} RIS element, the reflection phase shift is configured as: $e^{j\psi_i} = e^{j(\phi_A - \theta_{l,i})} = s_A e^{-j\theta_{l,i}}$, where $\theta_{l,i}$ is the phase of the channel between the i^{th} RIS element and antenna l, and $s_A = e^{j\phi_A}$ is the symbol chosen from the PSK constellation $\mathcal{M}_A$. The baseband signal synthesized by the i^{th} RIS element belonging to Partition 1 (i.e., $i \in \{1, 2, \ldots, N/2\}$ at any receive antenna r is given as:

$$\begin{aligned} x_{r,i} &= \sqrt{E} h_{r,i} e^{j\theta_{r,i}} \left(e^{j(\phi_A - \theta_{l,i})}\right) \\ &= \sqrt{E}\left(h_{r,i} e^{j(\theta_{r,i} - \theta_{l,i})}\right) s_A, \quad \forall i \in \{1, 2, \ldots, N/2\}. \end{aligned} \tag{2}$$

Partition 2: Similarly, for the i^{th} RIS element in the second partition, the reflection phase shift is configured as: $e^{j\psi_i} = e^{j(\phi_B - \theta_{m,i})} = s_B e^{-j\theta_{m,i}}$, where $\theta_{m,i}$ is the phase of the channel between the i^{th} RIS element and the second antenna in $\mathbf{p}$ (i.e., antenna m), and $s_B = e^{j\phi_B}$ is the modulation symbol chosen from the constellation $\mathcal{M}_B$. The baseband signal synthesized by the i^{th} RIS element belonging to Partition 2 (i.e., $i \in \left\{\frac{N}{2}+1, \ldots, N\right\}$) at any receive antenna r is given as:

$$\begin{aligned} x_{r,i} &= \sqrt{E} h_{r,i} e^{j\theta_{r,i}} \left(e^{j(\phi_B - \theta_{m,i})}\right) \\ &= \sqrt{E}\left(h_{r,i} e^{j(\theta_{r,i} - \theta_{m,i})}\right) s_B, \; \forall i \in \left\{\frac{N}{2}+1, \frac{N}{2}+2, \ldots, N\right\}. \end{aligned} \tag{3}$$

The overall synthesized signal at antenna r, resulting from the combined contributions of the independently tuned RIS

partitions, each comprising $N/2$ elements, is given as:

$$x_r = \sqrt{E}\left(s_A \sum_{i=1}^{N/2} h_{r,i} e^{j(\theta_{r,i}-\theta_{l,i})} + s_B \sum_{N/2+1}^{N} h_{r,i} e^{j(\theta_{r,i}-\theta_{m,i})}\right) \tag{4}$$

Considering AWGN, the received signal at any antenna r is the sum of synthesized signal x_r and noise n_r, i.e., $y_r = x_r + n_r$.

The maximum likelihood (ML) detector for RDM-RSM schemes is formulated as follows:

$$\left(\hat{\mathbf{p}}=(\hat{l},\hat{m}),\hat{s}_A,\hat{s}_B\right)$$

$$= \arg \min_{\mathbf{p}=(l,m),s_A,s_B} \sum_{r=1}^{N_R} |y_r - x_r(\mathbf{p}=(l,m),s_A,s_B)|^2, \tag{5}$$

where $x_r(\mathbf{p}=(l,m),s_A,s_B)$ is the synthesized signal, which depends on the selected permutation $\mathbf{p} = (l,m)$ and the modulation symbols s_A and s_B. Note that the ML detector in (5) is valid for both the RDM-RSMI and RDM-RSMJ schemes. In the case of RDM-RSMI, the signal x_r in (5) is synthesized as shown in (4), whereas for RDM-RSMJ, the signal x_r is synthesized as given in the expression (27).

B. Signal Analysis for RDM-RSMI Scheme

In the following, we analyze the received signals across various scenarios for the RDM-RSMI scheme. This analysis also aids in the development of a low-complexity detector that is applicable to both RDM-RSM schemes. For analytical convenience, we assume $E = 1$ in the following discussion; however, it will be reinstated later in the error performance analysis to account for SNR considerations.

Case 1: The received signal y_r at an erroneous antenna r (i.e., when $r \neq l$, and $r \neq m$) is given as:

$$y_r = \underbrace{s_A \sum_{i=1}^{N/2} h_{r,i} e^{j(\theta_{r,i}-\theta_{l,i})}}_{A_r} + \underbrace{s_B \sum_{\frac{N}{2}+1}^{N} h_{r,i} e^{j(\theta_{r,i}-\theta_{m,i})}}_{B_r} + n_r \tag{6}$$

Since $\theta_{r,i}$ is uniformly distributed in our model, the phase $(\theta_{r,i} - \theta_{l,i})$ modulo 2π for a given $\theta_{l,i}$ is also uniformly distributed in $[-\pi,\pi)$. Throughout this paper, we consider modulo 2π phase, and hence the phase RVs lie in $[-\pi,\pi)$. It follows that $h_{r,i}e^{j(\theta_{r,i}-\theta_{l,i})}$ is a CSCG RV following $\mathcal{CN}(0,1)$ for all i. By applying the central limit theorem (CLT) under the assumption of $\frac{N}{2} \gg 1$, we obtain $A_r \sim \mathcal{CN}\left(0,\frac{N}{2}\right)$. By similar reasoning, we get $B_r \sim \mathcal{CN}\left(0,\frac{N}{2}\right)$. Consequently, leveraging the properties of CSCG RVs, we find that $y_r \sim \mathcal{CN}(0, N+N_0)$. Thus, as desired, the tuning method of RDM-RSMI results in a zero-mean signal at the erroneous antenna. The real and imaginary components of the received signal at an incorrect antenna are distributed as:

$$\Re(y_r) \sim \mathcal{N}\left(0,\frac{N+N_0}{2}\right), \quad \Im(y_r) \sim \mathcal{N}\left(0,\frac{N+N_0}{2}\right). \tag{7}$$

Case 2: Here we consider the received signal y_r at the correct antenna r (i.e., when $r = l$ or $r = m$). The RDM-RSMI scheme enhances the received signal at both antennas in the selected permutation $\mathbf{p} = (l,m)$. At antenna $r = l$, the received signal y_l is expressed as follows:

$$y_l = \overbrace{\underbrace{s_A\left(\sum_{i=1}^{N/2} h_{l,i}\right)}_{A_l} + \underbrace{s_B \sum_{N/2+1}^{N} h_{l,i} e^{j(\theta_{l,i}-\theta_{m,i})}}_{B_l}}^{x_l} + n_l, \tag{8}$$

where $h_{l,i}$ is Rayleigh distributed with $\mathbb{E}\{h_{l,i}\} = \sqrt{\pi}/2$ and $\mathbb{V}\{h_{l,i}\} = (4-\pi)/4$. The RV A_l (which is real in this case) follows Gaussian distribution with a non-zero mean, given as:

$$A_l \sim \mathcal{N}\left(\frac{N\sqrt{\pi}}{4},\frac{N(4-\pi)}{8}\right), \quad B_l \sim \mathcal{CN}\left(0,\frac{N}{2}\right), \tag{9}$$

while the distribution of the complex RV B_l remains the same as B_r, given in the previous case.

With the RDM-RSMI scheme, the first partition of the RIS enhances the signal at the intended antenna l, aiding in the detection of both the correct antenna and the modulation symbol s_A. This enhancement is evident as the RV A_l in (9) has a non-zero mean, resulting in a higher energy signal at the correct antenna compared to the erroneous one, as observed in Case 1. Importantly, this increase in energy arises from the useful component of the signal carrying the symbol s_A. The second partition transmits symbol s_B toward its intended antenna m; however, this signal also reaches antenna l as indicated by the second term in (8). For brevity, we refer to this unintended signal component as *cross-antenna interference*—a term adopted in this work to effectively describe the operational perspective of our low-complexity, per-antenna detector, which treats signal components arising from unintended symbols at each antenna as unknown interference (not exploited by the detector). Since B_l is a CSCG RV (9), this unintended component raises the noise-plus-interference variance at antenna l to $N/2 + N_0$.

Due to symmetry, a similar analysis presented above for antenna l applies to the signal at the other target antenna m; however, the roles of the RIS partitions are reversed, as shown below:

$$y_m = \overbrace{\underbrace{s_A \sum_{i=1}^{N/2} h_{m,i} e^{j(\theta_{m,i}-\theta_{l,i})}}_{A_m} + \underbrace{s_B\left(\sum_{N/2+1}^{N} h_{m,i}\right)}_{B_m}}^{x_m} + n_m. \tag{10}$$

C. LC Detector Design for RDM-RSM Schemes

With the above signal analysis in perspective, we now introduce a two-stage LC detector. The first stage employs greedy detection (GD), which identifies the two receive antennas with the highest signal energy. The search space of GD includes only those antenna pairs $\{r, r'\}$ that correspond to the selected set of permutations. It is formulated as follows:

$$\{\hat{r},\hat{r}'\} = \arg \max_{\{r,r'\}} \left(|y_r|^2 + |y_{r'}|^2\right). \tag{11}$$

Here, $|y_r|^2$ and $|y_{r'}|^2$ represent the received signal energies at antennas r and r', respectively.

The second stage of the LC detector focuses on detecting the constellation symbols and, if necessary, determining the correct permutation for the previously identified antenna pair. Let $\mathbb{S}_{\hat{r},\hat{r}'}$ denote the set of valid or selected permutations associated with the above-identified antenna pair $\{\hat{r},\hat{r}'\}$. Depending on the permutation selection strategy employed during the design phase, $\mathbb{S}_{\hat{r},\hat{r}'}$ can take one of the following forms: $\{(\hat{r},\hat{r}'),(\hat{r}',\hat{r})\}$, $\{(\hat{r},\hat{r}')\}$ or $\{(\hat{r}',\hat{r})\}$. The symbols s_A, s_B and the permutation $\mathbf{p}=(l,m)$ can be jointly detected by applying the following coherent detector to the received signals on the antennas $\hat{r}$ and $\hat{r}'$:

$$\left\{\hat{s}_A,\hat{s}_B,(\hat{l},\hat{m})\right\}=\arg\min_{\substack{s_A,s_B\\(l,m)\in\mathbb{S}_{\hat{r},\hat{r}'}}}\left(|y_l-x_l|^2+|y_m-x_m|^2\right), \quad (12)$$

where the synthesized signals x_l and x_m are given in (8) and (10), respectively.

The coherent detector described in (12) involves significant implementation complexity due to the intensive computations required for the signal x_l in (8) and x_m in (10). For constant-envelope constellations and a single transmitted symbol, it is generally possible to transform a coherent detector into a low-complexity, non-coherent one without any loss in error performance. This is achieved by disregarding the weight of the transmitted symbol, which depends on the channel alongside other transmission parameters. However, in the case of the detector in (12), each synthesized signal involves two constellation symbols with different weights, making the above-mentioned transformation infeasible without performance loss. For example, x_l requires computing the weights of both s_A and s_B, as indicated in (8), with the weights differing due to the underlying channels. A similar argument applies to the signal x_m in (10).

In the following, we develop a non-coherent version of the detector given in (12), which significantly reduces complexity at the cost of a slight performance trade-off. To formulate this alternative detector, we analyze the received signal under the following scenarios:

Case 3: Here, we analyze the projection of the signal y_l (i.e., the signal at a correct antenna) onto an incorrect modulation symbol (i.e., when $\hat{s}_A\neq s_A$). From (8), the expression for $y_l\hat{s}_A^*$ is derived as follows:

$$y_l\hat{s}_A^*=y_le^{-j\hat{\phi}_A}=e^{j(\phi_A-\hat{\phi}_A)}\sum_{i=1}^{N/2}h_{l,i}+e^{j(\phi_B-\hat{\phi}_A)}\sum_{N/2+1}^{N}h_{l,i}e^{j(\theta_{l,i}-\theta_{m,i})}+n_le^{-j\hat{\phi}_A}. \quad (13)$$

Using (9) and (13), the distributions of the real and imaginary parts of $y_l\hat{s}_A^*$ can be expressed as follows:

$$\Re(y_l\hat{s}_A^*)\sim\mathcal{N}\left(\frac{N\sqrt{\pi}}{4}\cos\Delta\hat{\phi}_A,\frac{N(4-\pi)}{8}\cos^2\Delta\hat{\phi}_A+\frac{N}{4}+\frac{N_0}{2}\right),$$

$$\Im(y_l\hat{s}_A^*)\sim\mathcal{N}\left(\frac{N\sqrt{\pi}}{4}\sin\Delta\hat{\phi}_A,\frac{N(4-\pi)}{8}\sin^2\Delta\hat{\phi}_A+\frac{N}{4}+\frac{N_0}{2}\right),$$

where, $\Delta\hat{\phi}_A=\phi_A-\hat{\phi}_A$ in the above expressions.

Case 4: Here, we consider the projection of the signal y_l onto the correct modulation symbol (i.e., when $\hat{s}_A=s_A$), and we compare it with Case 3. Using (8), the expression for $y_ls_A^*$ is given as:

$$y_ls_A^*=y_le^{-j\phi_A}=\sum_{i=1}^{N/2}h_{l,i}+e^{j(\phi_B-\phi_A)}\sum_{\frac{N}{2}+1}^{N}h_{l,i}e^{j(\theta_{l,i}-\theta_{m,i})}+n_le^{-j\phi_A} \quad (14)$$

Using (9), and (14), we get the following:

$$\Re(\tilde{y}_l)=\Re(y_ls_A^*)\sim\mathcal{N}\left(\frac{N\sqrt{\pi}}{4},\frac{N(6-\pi)}{8}+\frac{N_0}{2}\right) \quad (15)$$

$$\Im(\tilde{y}_l)=\Im(y_ls_A^*)\sim\mathcal{N}\left(0,\frac{N}{4}+\frac{N_0}{2}\right) \quad (16)$$

It shows that the real component of $y_ls_A^*$, i.e., the projection of y_l, is maximized along the correct modulation symbol compared to the incorrect modulation symbol scenario in Case 3. By symmetry, the projection of y_m is also maximized along the correct symbol, i.e., when $\hat{s}_B=s_B$, and is given as $\Re(\tilde{y}_m)=\Re(y_ms_B^*)\sim\mathcal{N}\left(\frac{N\sqrt{\pi}}{4},\frac{N(6-\pi)}{8}+\frac{N_0}{2}\right)$.

Thus, the second stage of the proposed LC detector can apply the following non-coherent detector to the signals at the antennas $\{\hat{r},\hat{r}'\}$ that were detected in the first stage using GD:

$$\left\{\hat{s}_A,\hat{s}_B,(\hat{l},\hat{m})\right\}=\arg\max_{\substack{s_A,s_B\\(l,m)\in\mathbb{S}_{\hat{r},\hat{r}'}}}\left(\Re(y_ls_A^*)+\Re(y_ms_B^*)\right). \quad (17)$$

This non-coherent detector is a suboptimal version of the detector in (12), as it treats the signal component arising from unintended symbols at each antenna as unknown interference. In contrast, the detector in (12) jointly exploits both the intended and unintended signal components for detection at each selected antenna. Note that both steps of the LC detector in (11) and (17) are also valid for RDM-RSMJ, with the signals y_l and y_m synthesized by plugging $r=l$ and $r=m$ into (27), respectively.

IV. RDM-RSMJ: Design and Signal Analysis

RDM-RSMJ, a highly energy-efficient version of the RDM-RSM scheme, works by optimizing the reflection phase of each RIS element to maximize a well-defined objective function that considers the signals at both target antennas *jointly*. As a result, each and every RIS element contributes to enhancing the RF signal at both antennas while also transmitting both constellation symbols. This leads to a stronger received signal and an improved signal-to-interference-plus-noise ratio (SINR) at each antenna compared to the RDM-RSMI scheme, where only half of the RIS elements can serve each antenna.

A. RIS Reflection Coefficient Optimization for RDM-RSMJ

For analytical convenience, we begin by assuming that the RIS consists of a single element with a reflection coefficient $e^{j\psi}$, and we set $E=1$. The synthesized baseband signals at the receive antennas l and m are given as follows:

$$x_l=h_le^{j\theta_l}e^{j\psi},\quad x_m=h_me^{j\theta_m}e^{j\psi}. \quad (18)$$

The signals x_l and x_m are correlated due to the common reflection phase coefficient ψ. As a result, maximizing the

energy of each signal is not an independent task but a joint optimization problem. We formulate this problem below in an efficient manner, allowing for straightforward optimization.

As discussed earlier in the design of the LC detector, RDM-RSMI enhances the energy in the useful component of the synthesized signal that carries the modulation symbol, thereby improving symbol detection. Notably, it also results in boosting the overall synthesized signal at the correct antennas, thereby improving antenna detection simultaneously. Building on this concept, RDM-RSMJ further enhances the modulation symbol-carrying component of the synthesized signal, simultaneously increasing the overall signal strength. To achieve this, we concentrate on modulation symbol detection by leveraging the non-coherent detector in (17) and accordingly maximize $\Re(s_A^* x_l)$, and $\Re(s_B^* x_m)$ jointly as given below:

$$\Re(s_A^* x_l)+\Re(s_B^* x_m)= \Re\big(e^{-j\phi_A} h_l e^{j\theta_l} e^{j\psi}\big)+\Re\big(e^{-j\phi_B} h_m e^{j\theta_m} e^{j\psi}\big). \quad (19)$$

We aim to determine the optimal ψ that maximizes the objective function (19). This unconstrained optimization problem is solved by differentiating (19) with respect to ψ as follows:

$$\frac{d}{d\psi}\Big(\Re\big(e^{-j\phi_A} h_l e^{j\theta_l} e^{j\psi}\big)+\Re\big(e^{-j\phi_B} h_m e^{j\theta_m} e^{j\psi}\big)\Big)=0. \quad (20)$$

Using the identity $\Re(a)=\frac{a+a^*}{2}$ and performing some algebraic manipulations, we get:

$$e^{j\psi}=\frac{S}{|S|}=\frac{e^{j\phi_A} h_l e^{-j\theta_l}+e^{j\phi_B} h_m e^{-j\theta_m}}{|S|} \quad (21)$$

where

$$S=e^{j\phi_A} h_l e^{-j\theta_l}+e^{j\phi_B} h_m e^{-j\theta_m}. \quad (22)$$

We can rewrite (21) as $e^{j\psi}=s_A\left(\frac{h_l e^{-j\theta_l}}{|S|}\right)+s_B\left(\frac{h_m e^{-j\theta_m}}{|S|}\right)$.

Intuitively, this expression indicates that a given RIS element transmits both symbols s_A and s_B jointly, with the transmission weights being proportional to the channels associated with their respective intended antennas, l and m.

B. Signal Analysis for RDM-RSMJ Scheme

In this section, we analyze the received signals under various scenarios to understand the working of RDM-RSMJ. In each case, we begin with a single-element RIS and then generalize the findings to an RIS with N elements.

Case 1: We first consider the received signal y_r at an erroneous antenna r (i.e., when $r \neq l$ and $r \neq m$). The synthesized signal at antenna r is given as:$x_r = h_r e^{j\theta_r} e^{j\psi}$.

To analyze x_r, we need to determine the distribution of ψ. The reflection phase ψ of the RIS element tuned as $e^{j\psi} = S/|S|$ (21) is given below and is entirely determined by the phase of the RV S, as $|S|$ is merely a normalization factor to make the reflection amplitude equal to unity:

$$\psi=\angle S=\angle(e^{j\phi_A} h_l e^{-j\theta_l}+e^{j\phi_B} h_m e^{-j\theta_m}). \quad (23)$$

It is obvious that ψ is independent of channel $h_r e^{j\theta_r}$ in this case. Following the same argument as for (6), we find that S is CSCG and hence the modulo 2π phase of S, i.e., ψ is uniformly distributed in $[-\pi,\pi)$. As a result $x_r = h_r e^{j(\theta_r+\psi)}$ follows the same distribution as that of $h_r e^{j\theta_r}$ i.e., $x_r \sim \mathcal{CN}(0,1)$. Now, for the case of an RIS with N elements, the received signal at antenna r is:

$$y_r=\sum_{i=1}^{N} h_{r,i} e^{j\theta_{r,i}} e^{j\psi_i}+n_r. \quad (24)$$

The overall synthesized signal is the sum of i.i.d. signals reflected from N RIS elements, each following $\mathcal{CN}(0,1)$. Consequently, the received signal y_r follows:

$$y_r \sim \mathcal{CN}(0, N+N_0), \quad (25)$$

where N_0 is the noise power. The real and imaginary parts of y_r in this case are distributed as follows:

$$\Re(y_r)\sim\mathcal{N}\left(0,\frac{N+N_0}{2}\right), \quad \Im(y_r)\sim\mathcal{N}\left(0,\frac{N+N_0}{2}\right) \quad (26)$$

We observe that the signal distributions for the erroneous antenna remain the same in both the RDM-RSMI and RDM-RSMJ schemes. The received signal y_r (24) can alternatively be expressed by substituting $e^{j\psi_i}$ (the expression for $e^{j\psi_i}$ directly follows from (21) for the case when $N>1$) as:

$$y_r = x_r + n_r = s_A \underbrace{\sum_{i=1}^{N}\frac{h_{r,i}h_{l,i}e^{j(\theta_{r,i}-\theta_{l,i})}}{|S_i|}}_{A_r} + s_B \underbrace{\sum_{i=1}^{N}\frac{h_{r,i}h_{m,i}e^{j(\theta_{r,i}-\theta_{m,i})}}{|S_i|}}_{B_r} + n_r \quad (27)$$

where $S_i = e^{j\phi_A} h_{l,i} e^{-j\theta_{l,i}} + e^{j\phi_B} h_{m,i} e^{-j\theta_{m,i}}$ (directly follows from (22) for $N > 1$). Due to the symmetry of A_r and B_r, and since the sum of Gaussian RVs is also Gaussian, it follows from (25) that $A_r \sim \mathcal{CN}(0, N/2)$ and $B_r \sim \mathcal{CN}(0, N/2)$.

Case 2: Here we examine the received signal y_r at the correct antenna r (i.e., when $r = l$ or $r = m$). The tuning of RDM-RSMJ enhances the received signal at both target antennas in $\mathbf{p} = (l, m)$. Below, we analyze the received signal at antenna l only; due to symmetry, the same reasoning applies to the signal at antenna m as well. For antenna $r = l$, the synthesized signal x_l from a single-element RIS is expressed as:

$$x_l = h_l e^{j\theta_l} e^{j\psi} = s_A \frac{h_l^2}{|S|} + s_B \frac{h_l h_m e^{j(\theta_l-\theta_m)}}{|S|}. \quad (28)$$

At antenna l, the first term in (28) represents the useful signal for detecting s_A, while the second term accounts for the interference caused by the simultaneous transmission of s_B. For a single-element RIS, this interference is comparable in magnitude to the useful signal. However, when $N > 1$, as apparent in the received signal expression for y_l given below:

$$y_l = s_A \underbrace{\sum_{i=1}^{N}\frac{h_{l,i}^2}{|S_i|}}_{A_l} + s_B \underbrace{\sum_{i=1}^{N}\frac{h_{l,i}h_{m,i}e^{j(\theta_{l,i}-\theta_{m,i})}}{|S_i|}}_{B_l} + n_l, \quad (29)$$

the first term, being real and in phase, coherently adds up across all RIS elements. In contrast, the second term, being complex and having a random phase, does not add coherently across the RIS elements. As a result, the interference signal

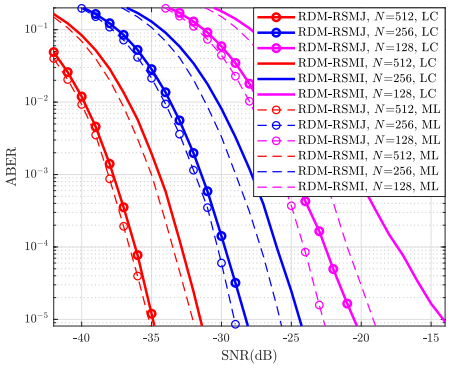


Fig. 2. Performance comparison: RDM-RSMJ vs RDM-RSMI, and ML vs LC detector at a bpcu of $b = 7$, with $N_R = 4$, $N_{\mathbf{p}} = 8$ and $M = 4$.

remains weak and does not scale in strength as N increases, unlike the useful signal. This observation is further supported by the following theorem, which investigates the distribution of the projection of the received signal y_l onto the correct modulation symbol $\hat{s}_A = s_A$.

Theorem 1: The real and imaginary parts of $y_l s_A^*$ under the RDM-RSMJ scheme follow the distributions:[1]

$$\Re(\tilde{y}_l) = \Re(y_l s_A^*) \sim \mathcal{N}\left(\frac{N\sqrt{\pi}}{2\sqrt{2}}, \frac{N(6-\pi)}{8} + \frac{N_0}{2}\right)$$
$$\Im(\tilde{y}_l) = \Im(y_l s_A^*) \sim \mathcal{N}\left(0, \frac{N}{4} + \frac{N_0}{2}\right)$$

Proof: The proof is given in Appendix A.■

Recognizing that the sum of Gaussian RVs remains Gaussian, we can show using Theorem 1 that the RVs A_l and B_l in (29) are distributed as follows:

$$A_l \sim \mathcal{N}\left(\frac{N\sqrt{\pi}}{2\sqrt{2}}, \frac{N(4-\pi)}{8}\right), \quad B_l \sim \mathcal{CN}\left(0, \frac{N}{2}\right) \tag{30}$$

By comparing these results with the RDM-RSMI scheme, we observe that RDM-RSMJ scheme boosts both the overall signal and the component of the signal carrying the modulation symbol at the intended antenna. This improvement is evident as the mean of $\Re(\tilde{y}_l)$ increases by a factor of $\sqrt{2}$, and by symmetry, the same holds for $\Re(\tilde{y}_m)$. Consequently, under the RDM-RSMJ scheme, both the GD and subsequent non-coherent detector experience a stronger signal at the intended antennas, resulting in enhanced detection performance.

Fig. 2 compares the ABER performance of the RDM-RSMI and RDM-RSMJ schemes at a reference value of $b = 7$ bpcu, where b denotes the total number of bits transmitted per symbol—that is, the sum of IM bits and conventionally-modulated bits. The simulation results are presented for three RIS configurations with N set to 128, 256, and 512. In all three setups, the number of receive antennas, N_R, is fixed at 4. Additionally, the number of antenna permutations, $N_{\mathbf{p}}$, is set to 8, enabling the transmission of 3 bits through IM, while the remaining 4 bits are transmitted via two simultaneous 4-PSK data streams (dual-mode) directed to a selected antenna pair. As expected, RDM-RSMJ consistently outperforms RDM-RSMI across all RIS configurations. Specifically, with the ML detector, RDM-RSMJ achieves an approximate 3 dB performance gain over RDM-RSMI in all cases. This improvement can be rightly attributed to the stronger received signal provided by RDM-RSMJ compared to RDM-RSMI, with a gain factor of $\sqrt{2}$, as established in Theorem 1.

[1]It is important to note that the distributions presented in Theorem 1 are approximate, as they are derived under the CLT assumption and involve additional approximations in the evaluation of their parameters (mean and variance), as detailed in Appendix A.

TABLE II
AN ILLUSTRATION OF COMPUTATION COMPLEXITY OF LC AND ML DETECTORS: NUMBER OF RMS REQUIRED FOR IMPLEMENTATION

b	$N_{\mathbf{p}}$	M	N	N_R	ML	LC
7	8	4	256	4	1058816	144
8	4	8	256	4	2117632	520

Fig. 2 also compares the performance of the proposed LC detector to that of the ML detector. For larger values of N, the LC detector demonstrates performance that is sufficiently closer to the ML detector for both RDM-RSM schemes. However, the LC detector approximates ML performance more closely for RDM-RSMJ than for RDM-RSMI. For example, at a BER of 10^{-5}, the performance gap between the ML and LC detectors is only 0.4 dB for RDM-RSMJ, compared to 0.8 dB for RDM-RSMI when $N = 512$. Another key observation from Fig. 2 is that the performance gap between the ML and LC detectors widens as the number of RIS elements decreases. This behavior can be attributed to the fundamental differences in how the two detectors exploit channel information. The ML detector uses a coherent detection algorithm that utilizes full CSI, enabling it to effectively capture and leverage channel variations across all RIS elements. In contrast, the LC detector is a non-coherent, energy-based detector that relies on the average received signal power. When N is large, the random small-scale fading effects (channel variations) across multiple RIS elements tend to average out, resulting in a more deterministic effective channel [31], [32]. Under such conditions, the LC detector's reliance on average power becomes more appropriate, and its performance approaches that of the ML detector. However, as the number of RIS elements decreases, this averaging effect diminishes, leading to increased channel variability, reducing the effectiveness of the LC detector compared to the ML detector.

Table II highlights the reduced computational complexity of the LC detector compared to the ML detector, measured in terms of real multiplications (RMs). This metric provides a practical and widely used basis for comparing algorithms at a high level, as it approximates computational cost regardless of specific hardware or implementation details [9], [28]. Using (5) and (4), it can be shown that the ML detector requires approximately $(4N+10)\cdot 2N_R N_{\mathbf{p}} M^2$ RMs. On the other hand, the two-stage LC detector requires only $2N_{\mathbf{p}} + 8M^2$ RMs, as derived from (11) and (17). For these evaluations, all the complex operations (e.g., complex multiplications, magnitude-squared operations) involved in the above-referenced equations are converted to their equivalent RM counts using standard rules (e.g., one complex multiplication equals four RMs, etc.).

Furthermore, among the benchmark schemes considered in this work, RIS-RQSSK [25] offers exceptionally low com-

putational complexity, requiring only $4N_R$ RMs for its GD based detector. For the two configurations listed in Table II, this amounts to just 16 RMs. However, a key limitation of RIS-RQSSK lies in its restricted SE under practical hardware constraints; for example, it cannot achieve SE beyond 6 bpcu in these configurations. In contrast, the proposed RDM-RSM schemes provide greater flexibility in supporting higher SE values, while still maintaining low computational complexity.

V. Theoretical Error Analysis

This section presents a theoretical analysis of the error performance for the proposed RDM-RSM schemes with the LC detector. The analysis primarily focuses on RDM-RSMJ, but since RDM-RSMI is a special case of RDM-RSMJ, the results are also applicable to RDM-RSMI with slight modifications, which will be explicitly mentioned if and where necessary.

A. Cumulative Average Bit Error Probability (ABEP)

The expression in (31), shown at the bottom of the page, provides an upper bound for evaluating the ABEP of data bits transmitted through both IM and conventional modulation in an RDM-RSM scheme (see, e.g., [8], [9], [33] for more details on ABEP evaluation for modulation schemes involving IM).

The term $\log_2(2MN_{\mathbf{p}})$ in the denominator accounts for the total number of bits transmitted per symbol. As represented by the two terms inside the brackets, the ABEP expression considers two error detection scenarios for each permutation $\mathbf{p}$:

(I) The term $P_c(\mathbf{p})2P_e^M$ accounts for the error contribution when the antenna permutation $\mathbf{p}$ is correctly detected with a probability $P_c(\mathbf{p})$, followed by the bit errors resulting from the erroneous detection of the two constellation symbols, approximated as $2P_e^M$ (assuming Gray encoding and neighboring symbol errors only). Here, P_e^M denotes the error probability of detecting the constellation symbol on the correct antenna. The probability $P_c(\mathbf{p})$ is evaluated as follows:

$$P_c(\mathbf{p}) = 1 - \sum_{\hat{\mathbf{p}}\neq\mathbf{p}} P_e(\mathbf{p}\to\hat{\mathbf{p}}),$$

where $P_e(\mathbf{p}\to\hat{\mathbf{p}})$ represents the PEP of detecting an incorrect permutation $\hat{\mathbf{p}}$ instead of $\mathbf{p}$.

(II) The second scenario, represented by the summation term, accounts for the error contribution when the permutation $\mathbf{p}$ is incorrectly detected as $\hat{\mathbf{p}}$ with a PEP $P_e(\mathbf{p}\to\hat{\mathbf{p}})$. In this scenario, two types of bit errors must be considered: i) Bit errors due to incorrect permutation detection, denoted as $e(\mathbf{p},\hat{\mathbf{p}})$, which corresponds to the Hamming distance between the binary representations of $\mathbf{p}$ and $\hat{\mathbf{p}}$; ii) Bit errors arising from erroneous detection of the constellation symbols at either one or both antennas, given as:

$$d_H(\mathbf{p},\hat{\mathbf{p}})\frac{\log_2 M}{2} + (2 - d_H(\mathbf{p},\hat{\mathbf{p}}))P_e^{\mathrm{M}}. \tag{32}$$

Since $\mathbf{p}\neq\hat{\mathbf{p}}$, the Hamming distance $d_H(\mathbf{p},\hat{\mathbf{p}})$ is either 1 or 2 for this scenario (but not 0, as that would indicate the correct permutation detection scenario). When $d_H(\mathbf{p},\hat{\mathbf{p}}) = 2$, both antennas are incorrectly detected, i.e., $\hat{l}\neq l$ and $\hat{m}\neq m$. Here we follow conservative approach, and assume that 50% of the bits transmitted to each antenna are in error, which amounts to $\frac{\log_2 M}{2}$ bits per antenna. Hence, for $d_H(\mathbf{p},\hat{\mathbf{p}}) = 2$, the expression in (32) reduces to $\log_2 M$ bits. When $d_H(\mathbf{p},\hat{\mathbf{p}}) = 1$, only one antenna is correctly detected. For the incorrectly detected antenna, we again assume that half of its bits are in error, i.e., $\frac{\log_2 M}{2}$ bits. For the correctly detected antenna, we estimate the constellation bit errors as P_e^{M}. Hence, for $d_H(\mathbf{p},\hat{\mathbf{p}}) = 1$, the expression in (32) reduces to $\frac{\log_2 M}{2} + P_e^M$ bit errors.

B. ABEP for Index Modulated Data (ABEP^{Im})

The following expression provides an upper bound for the ABEP of the IM data, i.e., the data bits transmitted through the indices of antenna permutations:

$$\mathrm{ABEP}^{\mathrm{IM}} \le \frac{1}{N_{\mathbf{p}}\log_2 N_{\mathbf{p}}}\sum_{\mathbf{p}}\sum_{\hat{\mathbf{p}}\neq\mathbf{p}} P_e(\mathbf{p}\to\hat{\mathbf{p}})e(\mathbf{p},\hat{\mathbf{p}}) \tag{33}$$

Both the cumulative and IM data ABEP expressions are based on the PEP for antenna permutations, $P_e(\mathbf{p}\to\hat{\mathbf{p}})$, expressed as follows:

$$\begin{aligned}P_e(\mathbf{p}\to\hat{\mathbf{p}}) = {} & P_e^A(\mathbf{p}\to\hat{\mathbf{p}})\mathbb{1}_A(\mathbf{p},\hat{\mathbf{p}}) \\ & + P_e^B(\mathbf{p}\to\hat{\mathbf{p}})\mathbb{1}_B(\mathbf{p},\hat{\mathbf{p}}) + P_e^C(\mathbf{p}\to\hat{\mathbf{p}})\mathbb{1}_C(\mathbf{p},\hat{\mathbf{p}})\end{aligned} \tag{34}$$

This is explained in detail in the following.

C. PEP Analysis for Antennas Permutation Detection

The PEP, $P_e(\mathbf{p}\to\hat{\mathbf{p}})$, depends on the relationship between the selected permutation $\mathbf{p}$ and the detected permutation $\hat{\mathbf{p}}$. We classify these relationships into three types based on the antennas used in $\mathbf{p}$ and $\hat{\mathbf{p}}$ and evaluate the PEP for each type accordingly: Type A: One antenna is common in both permutations $\mathbf{p}$ and $\hat{\mathbf{p}}$, regardless of its assigned mode/order. The indicator function $\mathbb{1}_A(\mathbf{p},\hat{\mathbf{p}})$ is 1 if $\mathbf{p}$ and $\hat{\mathbf{p}}$ are of type A, and 0 otherwise. In this case, $d_H(\mathbf{p},\hat{\mathbf{p}})$ can be either 1 or 2. Type B: None of the antennas are common in $\mathbf{p}$ and $\hat{\mathbf{p}}$, hence, $d_H(\mathbf{p},\hat{\mathbf{p}}) = 2$. Type C: $\mathbf{p}$ and $\hat{\mathbf{p}}$ are reverse permutations of each other, meaning they use the same antennas but with modes swapped. For type C, $d_H(\mathbf{p},\hat{\mathbf{p}}) = 2$. The PEP expressions for these three types are derived below in reverse order from their above listing to facilitate understanding.

1) Type C Error (Mode/Constellation Detection Error): For type C permutations $\mathbf{p}$ and $\hat{\mathbf{p}}$, the PEP $P_e^C(\mathbf{p}\to\hat{\mathbf{p}})$ is given as:

$$P_e^C(\mathbf{p}\to\hat{\mathbf{p}}) = P_c(\mathbb{I}_{\mathbf{p}})P_e^C\left(\mathbf{p}\to\hat{\mathbf{p}}|\mathbb{I}_{\mathbf{p}}\right) \tag{35}$$

$$\mathrm{ABEP} \le \frac{1}{\log_2(2MN_{\mathbf{p}})}\cdot\frac{1}{N_{\mathbf{p}}}\sum_{\mathbf{p}}\left[P_c(\mathbf{p})2P_e^M + \sum_{\hat{\mathbf{p}}\neq\mathbf{p}} P_e(\mathbf{p}\to\hat{\mathbf{p}})\left(e(\mathbf{p},\hat{\mathbf{p}}) + d_H(\mathbf{p},\hat{\mathbf{p}})\frac{\log_2 M}{2} + (2 - d_H(\mathbf{p},\hat{\mathbf{p}}))P_e^M\right)\right] \tag{31}$$

Since $\mathbf{p}$ and $\hat{\mathbf{p}}$ are reverse permutations of each other, they cannot be distinguished based on the received signal energy alone, as they use the same antennas but with their modes swapped (i.e., they are derived from the same index set $\mathbb{I}_{\mathbf{p}} = \mathbb{I}_{\hat{\mathbf{p}}}$). Thus, detecting a reversible permutation $\mathbf{p}$ (or $\hat{\mathbf{p}}$) is a two-step process: first, the corresponding index set $\mathbb{I}_{\mathbf{p}}$ (or $\mathbb{I}_{\hat{\mathbf{p}}}$) is identified using GD, followed by determining which of the its two reversible permutations was transmitted by determining the mode of each antenna. This is also reflected in the evaluation of $P_e^C(\mathbf{p} \to \hat{\mathbf{p}})$ (35), where $P_c(\mathbb{I}_{\mathbf{p}})$ (or $P_c(\mathbb{I}_{\hat{\mathbf{p}}})$) represents the probability of correctly detecting the index set $\mathbb{I}_{\mathbf{p}}$ (or $\mathbb{I}_{\hat{\mathbf{p}}}$). Given that $\mathbb{I}_{\mathbf{p}}$ is correctly detected, the $P_e^C\big(\mathbf{p} \to \hat{\mathbf{p}}|\mathbb{I}_{\mathbf{p}}\big)$ represents the conditional PEP that $\hat{\mathbf{p}}$ is detected when $\mathbf{p}$ was transmitted. The probability $P_c(\mathbb{I}_{\mathbf{p}})$ (which is the same as $P_c(\mathbb{I}_{\hat{\mathbf{p}}})$) is calculated as follows:

$$P_c(\mathbb{I}_{\mathbf{p}}) = P_c(\mathbb{I}_{\hat{\mathbf{p}}}) = 1 - \sum_{\tilde{\mathbf{p}} \neq \mathbf{p},\, \tilde{\mathbf{p}} \neq \hat{\mathbf{p}}} P_e(\mathbf{p} \to \tilde{\mathbf{p}}) \tag{36}$$

In the following, we derive the expression for the mode detection error, $P_e^C(\mathbf{p} \to \hat{\mathbf{p}}|\mathbb{I}_{\mathbf{p}})$. Constellation $\mathcal{M}_A$ is a rotated version of $\mathcal{M}_B$ by an angle of π/M, and vice versa. Consequently, each symbol in $\mathcal{M}_A$ has two neighboring symbols in $\mathcal{M}_B$, with phase shifts of $\pm\pi/M$ (one on either side), and the same holds for each symbol in constellation $\mathcal{M}_B$. Considering high SNR and accounting for neighboring inter-constellation symbol errors only, if the phase error exceeds π/M, one constellation will be mistakenly detected as the other. To characterize the type C error, we define the following condition: for permutation $\mathbf{p}$ not to be detected as its reverse permutation $\hat{\mathbf{p}}$, the constellation symbols at both antennas in $\mathbf{p}$ must not undergo a phase error greater than π/M. If the symbol at either antenna undergoes a phase error greater than π/M, a constellation detection error occurs with probability $P_e^C(\mathbf{p} \to \hat{\mathbf{p}}|\mathbb{I}_{\mathbf{p}})$. Note that the signals at both antennas are correlated. For the constellation $\mathcal{M}_A$ symbol $e^{j\phi_A}$ transmitted to antenna l, let $e^{j(\phi_A+\phi_1)}$ be one of its neighboring symbols in $\mathcal{M}_B$, with phase separation of ϕ_1. Similarly, for the constellation $\mathcal{M}_B$ symbol $e^{j\phi_B}$ transmitted to antenna m, let $e^{j(\phi_B+\phi_2)}$ be one of its neighboring symbols in $\mathcal{M}_A$, with phase separation of ϕ_2. Using the LC detector (17), the following expression provides the pairwise probability that both symbols $e^{j\phi_A}$ and $e^{j\phi_B}$ are correctly detected in relation to their inter-constellation neighboring symbols $e^{j(\phi_A+\phi_1)}$ and $e^{j(\phi_B+\phi_2)}$, respectively:

$$\begin{aligned}
&P\big(\Re(y_l e^{-j\phi_A}) + \Re(y_m e^{-j\phi_B}) \\
&\quad -\Re(y_l e^{-j(\phi_A+\phi_1)}) - \Re(y_m e^{-j(\phi_B+\phi_2)}) > 0\big) \\
&\quad = P\big(\Re(\tilde{y}_l) + \Re(\tilde{y}_m) - \Re(\tilde{y}_l e^{-j\phi_1}) - \Re(\tilde{y}_m e^{-j\phi_2}) > 0\big) \\
&= P(D_{\phi_1,\phi_2} > 0)
\end{aligned} \tag{37}$$

We can express D_{ϕ_1,ϕ_2} as $D_{\phi_1,\phi_2} = \mathbf{w}^T \mathbf{x}_{\phi_1,\phi_2}$, where vectors $\mathbf{w} = \big[1\ 1\ -1\ -1\big]^{\mathrm{T}}$, and $\mathbf{x}_{\phi_1,\phi_2}$ is given below:

$$\mathbf{x}_{\phi_1,\phi_2} = \big[\Re(\tilde{y}_l)\ \Re(\tilde{y}_m)\ \Re(\tilde{y}_l e^{-j\phi_1})\ \Re(\tilde{y}_m e^{-j\phi_2})\big]^{\mathrm{T}} \tag{38}$$

The mean vector and covariance matrix of $\mathbf{x}_{\phi_1,\phi_2}$ are given as:

$$\mathbf{m}_{\phi_1,\phi_2} = \big[\mu_R\ \mu_R\ \mu_R \cos\phi_1\ \mu_R \cos\phi_2\big]^{\mathrm{T}} \tag{39}$$

$$\mathbf{C}_{\phi_1,\phi_2} = \begin{bmatrix}
\sigma_R^2 & \sigma_{R,R} & \sigma_R^2 \cos\phi_1 & \sigma_{R,R}\cos\phi_2 \\
\sigma_{R,R} & \sigma_R^2 & \sigma_{R,R}\cos\phi_1 & \sigma_R^2\cos\phi_2 \\
\sigma_R^2\cos\phi_1 & \sigma_{R,R}\cos\phi_1 & \sigma_R^2\cos^2\phi_1 + \sigma_I^2\sin^2\phi_1 & \sigma_{3,4} \\
\sigma_{R,R}\cos\phi_2 & \sigma_R^2\cos\phi_2 & \sigma_{3,4} & \sigma_R^2\cos^2\phi_2 + \sigma_I^2\sin^2\phi_2
\end{bmatrix} \tag{40}$$

The mean μ_R and variances σ_R^2, σ_I^2 are derived in Appendix A, given in (70), (75) and (76), respectively. The covariances $\sigma_{R,R}$ and $\sigma_{I,I}$ are derived in appendices C and D, respectively. The remaining terms in $\mathbf{C}_{\phi_1,\phi_2}$ result from basic algebraic manipulations; for instance, $\sigma_{3,4}$ is expressed as follows:

$$\begin{aligned}
\sigma_{3,4} &= \mathbb{C}\{\Re(\tilde{y}_l e^{-j\phi_1}), \Re(\tilde{y}_m e^{-j\phi_2})\} \\
&= \mathbb{C}\{\Re(\tilde{y}_l)\cos\phi_1 + \Im(\tilde{y}_l)\sin\phi_1\,, \Re(\tilde{y}_m)\cos\phi_2 + \Im(\tilde{y}_m)\sin\phi_2\} \\
&= \sigma_{R,R}\cos\phi_1\cos\phi_2 + \sigma_{R,I}\cos\phi_1\sin\phi_2 \\
&\quad + \sigma_{R,I}\sin\phi_1\cos\phi_2 + \sigma_{I,I}\sin\phi_1\sin\phi_2 \\
&= \sigma_{R,R}\cos\phi_1\cos\phi_2 + \sigma_{I,I}\sin\phi_1\sin\phi_2
\end{aligned} \tag{41}$$

The simplification in (41) utilizes $\sigma_{R,I} = 0$ (Appendix B). For RDM-RSMI, Appendix E provides the expressions for μ_R (92), σ_R^2 (93), σ_I^2 (94), $\sigma_{R,R}$ (95), $\sigma_{I,I}$ (96) and $\sigma_{R,I}$ (97).

Since D_{ϕ_1,ϕ_2} is a linear combination of Gaussian RVs, therefore $D_{\phi_1,\phi_2} \sim \mathcal{N}(\mu_{D_{\phi_1,\phi_2}}, \sigma^2_{D_{\phi_1,\phi_2}})$, where

$$\mu_{D_{\phi_1,\phi_2}} = \mathbf{w}^T \mathbf{m}_{\phi_1,\phi_2}, \qquad \sigma^2_{D_{\phi_1,\phi_2}} = \mathbf{w}^T \mathbf{C}_{\phi_1,\phi_2} \mathbf{w}. \tag{42}$$

Hence, the probability that neither symbol undergoes a rotation to its neighboring symbols in the other constellation with phase shifts of ϕ_1 and ϕ_2 is given by:

$$P(D_{\phi_1,\phi_2} > 0) = Q\left(\frac{-\mu_{D_{\phi_1,\phi_2}}}{\sigma_{D_{\phi_1,\phi_2}}}\right) \tag{43}$$

In our model, each symbol in one constellation has two neighbors in the other constellation, with phase shifts $\pm\pi/M$. Hence, the constellation detection error is upper bounded as:

$$\begin{aligned}
P_e^C(\mathbf{p} \to \hat{\mathbf{p}} \mid \mathbb{I}_{\mathbf{p}}) &\leq \sum_{\phi_1 = \pm\frac{\pi}{M}} \sum_{\phi_2 = \pm\frac{\pi}{M}} P(D_{\phi_1,\phi_2} < 0) \\
&= \sum_{\phi_1 = \pm\frac{\pi}{M}} \sum_{\phi_2 = \pm\frac{\pi}{M}} Q\left(\frac{\mu_{D_{\phi_1,\phi_2}}}{\sigma_{D_{\phi_1,\phi_2}}}\right).
\end{aligned} \tag{44}$$

2) Type B Error: In this case, none of the antennas are common in the transmitted permutation $\mathbf{p}$ and the detected permutation $\hat{\mathbf{p}}$. The PEP $P_e^B(\mathbf{p} \to \hat{\mathbf{p}})$ is calculated as follows:

$$P_e^B(\mathbf{p} \to \hat{\mathbf{p}}) = P_e^B\big(\mathbf{p} \to \mathbb{I}_{\hat{\mathbf{p}}}\big) P_c(\hat{\mathbf{p}} \mid \mathbb{I}_{\hat{\mathbf{p}}}) \tag{45}$$

where $P_c(\hat{\mathbf{p}} \mid \mathbb{I}_{\hat{\mathbf{p}}})$ represents the probability of correctly detecting the permutation $\hat{\mathbf{p}}$, given that its corresponding index set $\mathbb{I}_{\hat{\mathbf{p}}}$ is detected. If the detected permutation $\hat{\mathbf{p}}$ is not reversible (i.e., its reverse is not among the chosen permutations), then $P_c(\hat{\mathbf{p}} \mid \mathbb{I}_{\hat{\mathbf{p}}}) = 1$. In this case, the PEP simplifies to:

$$P_e^B(\mathbf{p} \to \hat{\mathbf{p}}) = P_e^B\big(\mathbf{p} \to \mathbb{I}_{\hat{\mathbf{p}}}\big) \tag{46}$$

This follows from the fact that for non-reversible permutations, detecting the index set alone is sufficient. For a reversible

permutation $\hat{\mathbf{p}}$, where both permutations of $\mathbb{I}_{\hat{\mathbf{p}}}$ are valid, we adopt a conservative approach and assume $P_c(\hat{\mathbf{p}} \mid \mathbb{I}_{\hat{\mathbf{p}}}) = 0.5$.

Based on GD, the expression for $P_e^B(\mathbf{p} \to \mathbb{I}_{\hat{\mathbf{p}}})$ is derived as follows:

$$\begin{aligned} P_e^B(\mathbf{p} \to \mathbb{I}_{\hat{\mathbf{p}}}) &= P(|y_l|^2 + |y_m|^2 - |y_{\hat{l}}|^2 - |y_{\hat{m}}|^2 < 0) \\ &= P(|\tilde{y}_l|^2 + |\tilde{y}_m|^2 - |\tilde{y}_{\hat{l}}|^2 - |\tilde{y}_{\hat{m}}|^2 < 0) \\ &= P\big((\tilde{y}_l^{\Re})^2 + (\tilde{y}_l^{\Im})^2 + (\tilde{y}_m^{\Re})^2 + (\tilde{y}_m^{\Im})^2 \\ &\quad - (\tilde{y}_{\hat{l}}^{\Re})^2 - (\tilde{y}_{\hat{l}}^{\Im})^2 - (\tilde{y}_{\hat{m}}^{\Re})^2 - (\tilde{y}_{\hat{m}}^{\Im})^2 < 0\big) \\ &= P(D < 0). \end{aligned} \tag{47}$$

It is evident that the order of antennas in both $\mathbf{p}$ and $\hat{\mathbf{p}}$ is irrelevant in the derivation of (47). Unfortunately, the real parts of the received signals on the correct antennas i.e., $\tilde{y}_l^{\Re}$ and $\tilde{y}_m^{\Re}$ are correlated, and similarly imaginary parts $\tilde{y}_l^{\Im}$ and $\tilde{y}_m^{\Im}$ are also correlated. Therefore, we express D in quadratic form of Gaussian RVs to derive its statistics. Consequently, $D = \mathbf{x}^T\mathbf{W}\mathbf{x}$, where vector $\mathbf{x}$ and matrix $\mathbf{W}$ are given below:

$$\mathbf{x} = \begin{bmatrix} \tilde{y}_l^{\Re} & \tilde{y}_l^{\Im} & \tilde{y}_m^{\Re} & \tilde{y}_m^{\Im} & \tilde{y}_{\hat{l}}^{\Re} & \tilde{y}_{\hat{l}}^{\Im} & \tilde{y}_{\hat{m}}^{\Re} & \tilde{y}_{\hat{m}}^{\Im} \end{bmatrix}^{\mathrm{T}} \tag{48}$$

$$\mathbf{W} = \mathrm{diag}\begin{bmatrix} 1 & 1 & 1 & 1 & -1 & -1 & -1 & -1 \end{bmatrix} \tag{49}$$

The mean vector and covariance matrix of $\mathbf{x}$ are calculated as:

$$\mathbf{m} = \begin{bmatrix} \mu_R & 0 & \mu_R & 0 & 0 & 0 & 0 & 0 \end{bmatrix}^{\mathrm{T}} \tag{50}$$

$$\mathbf{C} = \begin{bmatrix} \sigma_R^2 & 0 & \sigma_{R,R} & 0 & 0 & 0 & 0 & 0 \\ 0 & \sigma_I^2 & 0 & \sigma_{I,I} & 0 & 0 & 0 & 0 \\ \sigma_{R,R} & 0 & \sigma_R^2 & 0 & 0 & 0 & 0 & 0 \\ 0 & \sigma_{I,I} & 0 & \sigma_I^2 & 0 & 0 & 0 & 0 \\ 0 & 0 & 0 & 0 & \sigma_e^2 & 0 & 0 & 0 \\ 0 & 0 & 0 & 0 & 0 & \sigma_e^2 & 0 & 0 \\ 0 & 0 & 0 & 0 & 0 & 0 & \sigma_e^2 & 0 \\ 0 & 0 & 0 & 0 & 0 & 0 & 0 & \sigma_e^2 \end{bmatrix} \tag{51}$$

The expressions for μ_R, σ_R^2, σ_I^2, $\sigma_{R,R}$, and $\sigma_{I,I}$ are previously discussed for the covariance matrix in (39). The variances of the real and imaginary parts of the signal at the erroneously detected antenna are equal as given in (26), and can be expressed for the signal with energy E as follows:

$$\sigma_e^2 = (NE + N_0)/2. \tag{52}$$

The above expression of σ_e^2 remains the same for the RDM-RSMI case, which directly follows from (7).

The MGF of D is calculated as follows:

$$\begin{aligned} M_D(s) &= (\det(\mathbf{I} - 2s\mathbf{W}\mathbf{C}))^{-\frac{1}{2}} \\ &\quad \times \exp\left(-\frac{1}{2}\mathbf{m}^{\mathrm{T}}\left[\mathbf{I} - (\mathbf{I} - 2s\mathbf{W}\mathbf{C})^{-1}\right]\mathbf{C}^{-1}\mathbf{m}\right) \end{aligned} \tag{53}$$

The CF of D i.e., $\Psi_D(\omega)$ can be found from the above equation by replacing s with $j\omega$. The following Gil-Pelaez's inversion formula for $d = 0$ can be used to calculate the PEP:

$$F_D(d) = \frac{1}{2} - \int_0^{\infty} \frac{\Im\left\{e^{-jwd}\Psi_D(w)\right\}}{w\pi} dw \tag{54}$$

where $F_D(d) = P(D < d)$ is the CDF and $\Psi_D(\omega) = \mathbb{E}[e^{j\omega D}]$ is the CF of D.

3) Type A Error: In this case, one of the antennas is common in the transmitted permutation $\mathbf{p}$ and the detected permutation $\hat{\mathbf{p}}$, regardless of its assigned mode/order. The PEP $P_e^A(\mathbf{p} \to \hat{\mathbf{p}})$ is calculated as follows:

$$P_e^A(\mathbf{p} \to \hat{\mathbf{p}}) = P_e^A(\mathbf{p} \to \mathbb{I}_{\hat{\mathbf{p}}}) P_c(\hat{\mathbf{p}} \mid \mathbb{I}_{\hat{\mathbf{p}}}) \tag{55}$$

To derive the expression for $P_e^A(\mathbf{p} \to \mathbb{I}_{\hat{\mathbf{p}}})$, we assume, without loss of generality, that $m = \hat{m}$. However, the derived error expression remains the same for all four possible type A cases ($l = \hat{l}$, or $l = \hat{m}$, or $m = \hat{m}$, or $m = \hat{l}$). We apply the same approach used for type B error evaluation, but in this case, the signals on m and $\hat{m}$ effectively cancel each other out in the expression for D since they correspond to the same antenna.

$$\begin{aligned} P_e^A(\mathbf{p} \to \mathbb{I}_{\hat{\mathbf{p}}}) &= P(|y_l|^2 - |y_{\hat{l}}|^2 < 0) = P(|\tilde{y}_l|^2 - |\tilde{y}_{\hat{l}}|^2 < 0) \\ &= P((\tilde{y}_l^{\Re})^2 + (\tilde{y}_l^{\Im})^2 - (\tilde{y}_{\hat{l}}^{\Re})^2 - (\tilde{y}_{\hat{l}}^{\Im})^2 < 0) = P(D < 0) \end{aligned} \tag{56}$$

We can express D in quadratic form of Gaussian RVs as $D = \mathbf{x}^T\mathbf{W}\mathbf{x}$, where vector $\mathbf{x}$ and matrix $\mathbf{W}$ are defined as:

$$\mathbf{x} = \begin{bmatrix} \tilde{y}_l^{\Re} & \tilde{y}_l^{\Im} & \tilde{y}_{\hat{l}}^{\Re} & \tilde{y}_{\hat{l}}^{\Im} \end{bmatrix}^{\mathrm{T}}, \quad \mathbf{W} = \mathrm{diag}\begin{bmatrix} 1 & 1 & -1 & -1 \end{bmatrix}$$

The mean vector and covariance matrix of $\mathbf{x}$ are given as:

$$\mathbf{m} = \begin{bmatrix} \mu_R & 0 & 0 & 0 \end{bmatrix}^{\mathrm{T}}, \quad \mathbf{C} = \mathrm{diag}\begin{bmatrix} \sigma_R^2 & \sigma_I^2 & \sigma_e^2 & \sigma_e^2 \end{bmatrix}$$

The remaining steps are the same as for the type B error.

D. Error Analysis for Constellation Symbol Detection, P_e^M

Without loss of generality, we assume in this section that antenna l is correctly detected, i.e., $\hat{l} = l$, while antenna m is incorrectly detected, i.e., $\hat{m} \neq m$. For the correctly detected antenna $\hat{l}$, we evaluate the modulated bits errors as P_e^{M} considering Gray encoding and neighboring symbol errors only. For the incorrectly detected antenna $\hat{m}$, we simply assume half of its bits are in error. The SINR at the correctly detected antenna $\hat{l} = l$ is given as $\gamma = \frac{A_l^2 E}{N_I}$,

where N_I is the noise-plus-interference power, expressed as $N_I = N_0 + \frac{EN}{2}$. Here, N_0 is AWGN, while $\frac{EN}{2}$ is due to the interference at the antenna l caused by the signal reflected by the RIS for the other correct antenna m, shown by RV B_l in (30). The RV A_l is Gaussian as given in (30), so A_l^2 and, consequently, γ are non-central chi-squared RVs with one degree of freedom. The MGF of the RV γ is given as [34]:

$$M_\gamma(s) = \left(1 - 2s\sigma^2\right)^{-\frac{1}{2}} e^{\frac{s\mu^2}{1-2s\sigma^2}} \tag{57}$$

where σ^2 is identical for both RDM-RSM schemes given as:

$$\sigma^2 = \mathbb{V}\left\{A_l\sqrt{E/N_I}\right\} = EN(4-\pi)/8N_I \tag{58}$$

For the RDM-RSMI scheme, μ^2 is given as (RV A_l from 9):

$$\mu^2 = \mathbb{E}\left\{A_l\sqrt{E/N_I}\right\}^2 = EN^2\pi/16N_I. \tag{59}$$

For the RDM-RSMJ, scheme μ^2 is given as (RV A_l from 30):

$$\mu^2 = \mathbb{E}\left\{A_l\sqrt{E/N_I}\right\}^2 = EN^2\pi/8N_I \tag{60}$$

Finally, the average symbol error probability (SEP) for M-PSK evaluated independently at one antenna is given as [35]:

$$P_e^M = \frac{1}{\pi}\int_0^{\frac{(M-1)\pi}{M}} M_\gamma\left(\frac{-\sin^2(\pi/M)}{\sin^2\eta}\right) d\eta. \tag{61}$$

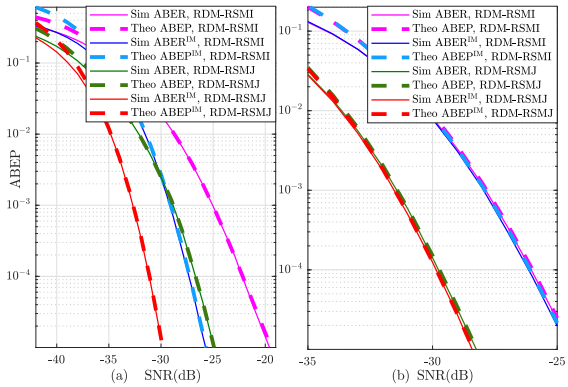


Fig. 3. Theoretically evaluated cumulative-ABEP and ABEP$^{\text{IM}}$ results are validated by simulations. (a) $b = 8$, $N_{\mathbf{p}} = 4$, $M = 8$. (b) $b = 7$, $N_{\mathbf{p}} = 8$, $M = 4$.

At high SNR, with Gray encoding and considering nearest-neighbor errors, it is customary to assume that the error bits are approximately given by the SEP, P_e^M.

Figs. 3(a) and 3(b) validate the accuracy of the analytical expressions for cumulative-ABEP (31) and ABEP$^{\text{IM}}$ (33) through simulation results across two diverse configurations with $N_R = 4$. The configuration of Fig. 3(a), results in ABER$^{\text{IM}}$ being significantly lower than ABER due to a low $N_{\mathbf{p}}$, with only 2 bits transmitted via IM and 6 bits via PSK streams. Both ABEP and ABEP$^{\text{IM}}$ serve as tight upper bounds for ABER and ABER$^{\text{IM}}$, respectively, at higher SNR for both RDM-RSM schemes. Fig. 3(b) demonstrates this validation in a different configuration where $N_{\mathbf{p}}$ is increased to 8 and M is reduced to 4. Additionally, this setup utilizes reversible permutations, unlike the earlier setup. Here, 3 bits are transmitted via IM compared to 4 bits via PSK, achieving a balanced trade-off. In this setup, ABER and ABER$^{\text{IM}}$ are comparatively close to each other and also align well with the analytical results.

VI. Comparative Analysis

In this section, we analyze the performance of the proposed RDM-RSM in terms of ABER plotted against SNR. Similar to conventional diversity combining and SM schemes, we treat E_s/N_0 as SNR. To ensure clarity, as commonly done, we exclude the consideration of large-scale path loss, as it is implicitly accounted for in the received SNR.

Fig. 4 shows the ABER of the RDM-RSMJ scheme for three different setups, with N_R set to 2, 4, and 8, and compares it with several benchmark modulation schemes over a bpcu range of 4 to 10 bits. RIS-RQSSK [25] is one of the benchmark schemes, which is efficient in terms of ABER performance but constrained by the bpcu limit imposed by N_R, achieving a maximum bpcu of $2\log_2(N_R)+2$. Therefore, the number of antennas needs to be varied across the three setups to enable a fair comparison with RIS-RQSSK at different bpcu values. RIS-SM-PSK [9], another benchmark scheme, is considered because it can support any bpcu value for a given N_R, similar to our proposed scheme. Additionally, RIS-SM with QAM [36], though it is not fully compatible with our RIS-AP model, is included as it provides a valuable reference. Notably, RIS-SM-QAM, unlike all other schemes in the figure, utilizes the RIS for IM only, while its conventionally modulated symbol (QAM in this case) is generated at the RF source. To ensure a fair comparison, it is important to highlight that all modulation schemes presented in Fig. 4 employ their respective GD-based LC detectors proposed in their original studies. Notably, although RIS-SM-QAM uses a GD detector for antenna detection, it additionally requires partial CSI at the second stage for QAM symbol detection [36]—this is indicated by the label "GD-P" in the Fig. 4 legend.

We begin the error analysis of RDM-RSMJ in a setup featuring only two receive antennas ($N_R = 2$), as illustrated by ABER plots in Fig. 4(a). RDM-RSMJ significantly outperforms RIS-SM-PSK and RIS-SM-QAM at bpcu values of 4, 5, and 6. The improved performance can be explained by noting that RDM-RSMJ splits the data into two PSK streams, each with a lower modulation order compared to that of the reference RIS-SM schemes. Additionally, both streams benefit from joint-amplification provided by RDM-RSMJ, boosting the received signal at each antenna. Notably, RIS-SM-QAM requires partial CSI for the constellation symbol detection, whereas RIS-SM-PSK, RDM-RSMJ, and RIS-RQSSK do not need CSI for detection. Moreover, as we will see in the following two setups, RDM-RSMJ's performance can be further enhanced by increasing the proportion of data transmitted via IM. However, in this setup, IM does not play a major role in data transmission, as most bits are carried by dual-mode PSK streams, with a maximum of only 1 bit transmitted via IM by setting $N_{\mathbf{p}}$ to its upper limit of 2. This figure also makes a comparison with RIS-RQSSK, which achieves performance close to RDM-RSMJ at a bpcu of 4. However, RIS-RQSSK suffers from the limitation that it cannot support bpcu values higher than 4 in this setup; therefore, we have to increase N_R to extend its achievable bpcu value beyond 4.

Figs. 4(b) and 4(c) further illustrate that RDM-RSMJ consistently outperforms the benchmark schemes, which either suffer from limited bpcu or exhibit poor error performance. These figures correspond to setups with 4 and 8 receive antennas, respectively. In these configurations, the number of bits transmitted via IM can be increased to a maximum of 3 and 5 by selecting up to 8 and 32 antenna permutations, respectively. With data now divided more evenly between IM and conventionally modulated data streams, RDM-RSMJ exhibits a significant performance advantage over both RIS-SM schemes across bpcu values ranging from 6 to 10. While RIS-RQSSK shows competitive ABER performance, it is limited to a maximum bpcu of 6 and 8 in these two setups. In contrast, RDM-RSMJ can flexibly adjust the number of antenna permutations $N_{\mathbf{p}}$ and the modulation order M of the PSK streams to support a wide range of bpcu values while maintaining an improved ABER.

Using Figs. 4(a) and 4(b), we highlight some interesting insights regarding the performance gains achieved by increasing the number of receive antennas, which allows transmitting more bits via IM. In Fig. 4(a), RDM-RSMJ achieves a target ABER of 10^{-5} at an SNR of approximately -25 dB for a bpcu of 6. Here, all 6 bits are transmitted via dual-mode PSK streams, each with $M = 8$, and no bits are allocated to IM,

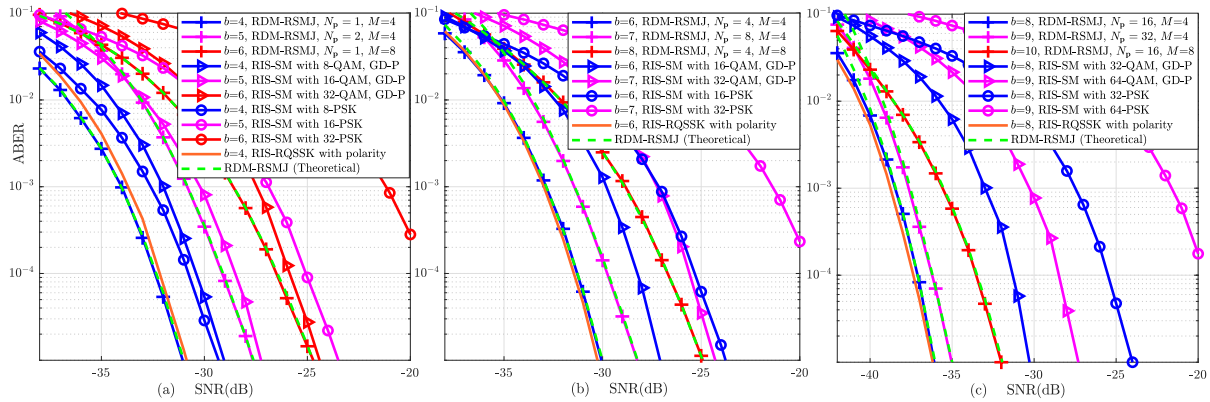


Fig. 4. ABER performance of the RDM-RSMJ scheme at various bpcu values ranging from 4 to 10 with (a) $N_R = 2$, and $N = 256$. (b) $N_R = 4$, and $N = 256$. (c) $N_R = 8$, and $N = 512$. Comparisons with relevant modulation schemes are also provided.

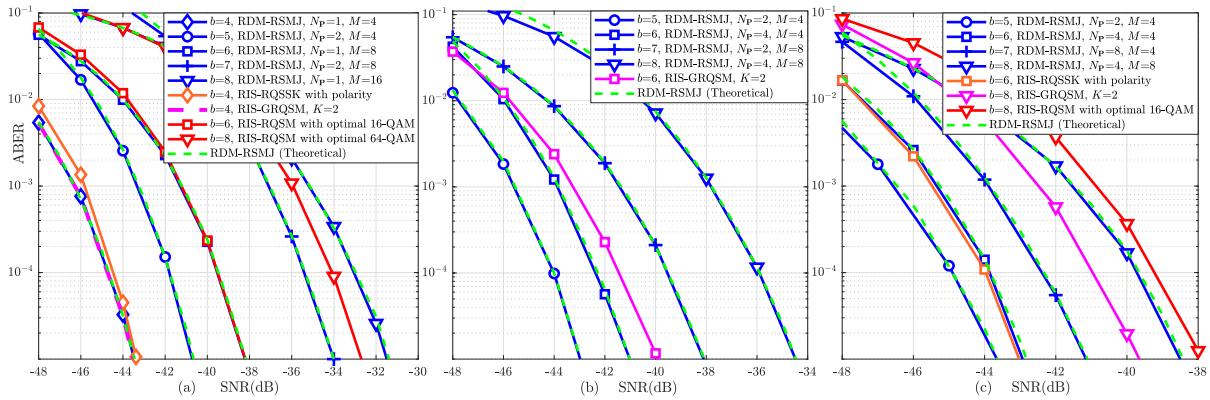


Fig. 5. ABER performance of the RDM-RSMJ scheme at bpcu values ranging from 4 to 8 with (a) $N_R = 2$, (b) $N_R = 3$, (c) $N_R = 4$, where $N = 1024$. Comparisons with RIS-RQSSK, RIS-GRQSM, and RIS-RQSM are also included at their respective supported bpcu values within the considered range.

as $N_{\mathbf{p}} = 1$. On the other hand, Fig. 4(b) shows that RDM-RSMJ achieves the same ABER at a similar SNR but for a higher bpcu of 8. In this setup, 2 bits are transmitted via IM using 4 antenna permutations, while the remaining 6 bits are carried by the dual-mode PSK streams, still with $M = 8$. Both setups utilize the same number of RIS elements, $N = 256$. This highlights the importance of carefully selecting system parameters to strike a balance between the bits allocated to IM and those transmitted through conventionally modulated streams. Such a balance is essential for enhancing the overall ABER performance under hardware constraints, such as the number of receive antennas.

Fig. 5 further illustrates the capability of the RDM-RSMJ scheme to programmably support a continuous range of bpcu values under the hardware constraint of a fixed number of receive antennas in each setup, while maintaining robust ABER performance. As an example, the figure specifically shows that the RDM-RSMJ scheme can achieve bpcu values across the considered range from 4 to 8 by configuring M and $N_{\mathbf{p}}$ for the three setups with a limited N_R of 2, 3, and 4. For benchmarking, two additional state-of-the-art modulation schemes are included in the figure: RIS-GRQSM [26] and RIS-RQSM [8]. As an extension of the RIS-RQSSK framework [25], RIS-GRQSM inherits its fundamental design principles and relies primarily on IM, thereby exhibiting excellent ABER performance. Furthermore, it can support higher bpcu values of $2\left(K + \left\lfloor \log_2 \binom{N_R}{K} \right\rfloor\right)$, where $K \leq N_R$. Nevertheless, its maximum achievable bpcu value remains inherently constrained by the number of receive antennas; therefore, these three setups with different N_R values in Fig. 5 are chosen to enable a fair comparison with the RDM-RSMJ scheme at bpcu values of 4, 6 and 8.

Fig. 5(a) considers the setup with $N_R = 2$, where both RIS-RQSSK and RIS-GRQSM can achieve a maximum bpcu value of 4. The ABER performance of RDM-RSMJ closely matches that of both reference schemes at this bpcu value. The key distinction, however, is that RDM-RSMJ can reliably support higher bpcu values without increasing N_R, as shown by its ABER curves for bpcu values ranging from 4 to 8.

In the setup of Fig. 5(b), N_R is increased to 3 so that RIS-GRQSM can support a bpcu of 6. RIS-RQSSK is not included in this comparison, as its design typically assumes N_R to be a power of 2. The figure shows that RDM-RSMJ achieves better ABER performance than RIS-GRQSM at this bpcu value, and the reason can be explained as follows. At this bpcu value, both schemes transmit the same number of bits via IM (2 bits). RIS-GRQSM transmits the remaining 4 bits by modulating the signal polarities, whereas RDM-RSMJ splits them into two PSK streams, each with a lower modulation order of $M = 4$ (QPSK). Notably, both modula-

tion choices (QPSK and polarity modulation) for transmitting these remaining 4 bits offer comparable robustness in terms of BER performance. It is important to highlight that both RDM-RSMJ and RIS-GRQSM employ LC detectors that perform per-antenna detection, treating the signal components arising from the unintended symbols at each antenna as unknown interference, as discussed previously. The performance of these LC detectors is influenced by this cross-antenna interference, whose power generally increases as the number of selected antennas grows. In this setup, RDM-RSMJ selects only two receive antennas, whereas RIS-GRQSM may select up to three. As a result, the cross-antenna interference level at some selected antennas can be higher in RIS-GRQSM, thereby affecting the detection performance. This explains the ABER advantage of RDM-RSMJ over RIS-GRQSM in this specific case, where other transmission parameters are comparable.

Next, by adjusting M and $N_{\mathbf{P}}$, Fig. 5(b) further illustrates the ABER performance of RDM-RSMJ across a bpcu range from 5 to 8. It can be noticed that at each bpcu value, RDM-RSMJ performs better in Fig. 5(b) compared to Fig. 5(a). This improvement can be attributed to the increased flexibility provided by the higher number of receive antennas, enabling the transmission of more bits via IM and thereby lowering the required modulation order M.

Fig. 5(c) features $N_R = 4$, where RIS-RQSSK can achieve a maximum bpcu of 6. At this bpcu value, both RDM-RSMJ and RIS-RQSSK exhibit nearly identical ABER performance. Compared to RIS-RQSSK, RIS-GRQSM can support higher bpcu values in this setup. Indeed, as discussed in [26], RIS-GRQSM proves to be a highly efficient scheme for larger N_R, with both its achievable bpcu and ABER performance improving significantly as N_R increases. This is also evident in Fig. 5(c), where RIS-GRQSM performs better than RDM-RSMJ at a bpcu value of 8. For even larger N_R, RIS-GRQSM can consistently provide better ABER than RDM-RSMJ, though only at its supported bpcu values. This advantage in terms of ABER performance stems from its design principle, which primarily relies on the efficient utilization of IM, allowing RIS-GRQSM to transmit more bits through antenna indices as N_R grows, compared to RDM-RSMJ. However, this comes with the trade-off that its maximum bpcu remains inherently limited by N_R. In contrast, while RDM-RSMJ also utilizes IM, it deliberately trades part of its IM capacity for the flexibility offered by dual-mode PSK, enabling it to programmably support higher bpcu values without increasing N_R. Finally, Fig. 5(c) shows that the performance of RDM-RSMJ at each bpcu value from 5 to 8 is further improved compared to both Figs. 5(a) and 5(b), owing to the higher N_R in this setup, as discussed earlier.

The authors who introduced RIS-GRQSM [26] and RIS-RQSSK [25] also proposed RIS-RQSM [8], which is included as an additional benchmark in Fig. 5. In RIS-RQSM, however, the achievable bpcu can be increased without necessarily increasing N_R, as data is encoded not only in the antenna indices but also by modulating the amplitudes of the real and imaginary components of the signals at the two selected receive antennas, corresponding to the transmitted QAM symbol.

Since the design of RIS-RQSM in [8] typically considers N_R to be a power of two and employs only square QAM constellations (not rectangular ones), it is benchmarked only in Figs. 5(a) and 5(c), and only at even bpcu values within the considered range. Fig. 5(a) shows that the ABER of RDM-RSMJ and RIS-RQSM is nearly identical at a bpcu of 6, while at 8, RIS-RQSM performs better. This is because, with $N_R = 2$, RDM-RSMJ can transmit only 1 bit via IM, which aligns inherently with odd bpcu targets but cannot be exploited at even bpcu values, as shown in the figure. Nevertheless, even without IM at even bpcu values in this limiting setup, RDM-RSMJ still achieves competitive performance due to its key feature of intelligently tuning the RIS to efficiently transmit data over two parallel lower-order dual-mode PSK streams. When N_R is increased to 4, as shown in Fig. 5(c), RDM-RSMJ performs better than RIS-RQSM at a bpcu of 8, since here IM can also be utilized for even bpcu targets by carrying 2 bits. For odd bpcu values, 1 or 3 bits can be transmitted via IM, as shown in the figure.

Considering their ability to support higher bpcu values without solely relying on increasing the number of receive antennas, both RDM-RSMJ and RIS-RQSM demonstrate robust ABER performance, as illustrated in Figs. 5(a) and 5(c)—for even bpcu values in RIS-RQSM and for all bpcu values in RDM-RSMJ within the considered range. However, it is important to highlight that, unlike our RDM-RSMJ system model, RIS-RQSM requires additional hardware to control and vary the RF signal power at the source. This fine RF power control is necessary for two reasons: first, RIS-RQSM employs QAM constellations—in fact, customized QAM constellations adaptively tailored based on the underlying channel SNR for improved performance; second, it requires a one-tap ZF pre-equalizer at the transmitter side. Both these tasks demand dynamic and precise RF power control at the source. In contrast, RDM-RSMJ avoids these requirements—eliminating the need for active hardware control—and relies solely on the intelligent tuning of the passive RIS for its operation to maintain a low-complexity transmitter design while providing programmable bpcu values and enhanced ABER performance. Moving forward, the RDM-RSMJ framework introduced in this article can naturally be extended to develop a generalized RIS-based multi-mode RSM scheme that allows a more flexible interplay between IM and multi-mode PSK streams for data transmission, enabling further performance improvements while preserving the inherent low complexity of the system.

VII. Conclusion and Future Work

In this article, we introduced RDM-RSM, a modulation scheme designed to improve both the SE and error performance of RIS-APs. Two versions were proposed: RDM-RSMI, which enhances the received signals at the two selected antennas independently, and RDM-RSMJ, which further improves the energy efficiency of RDM-RSMI by enhancing the signals at both antennas jointly, resulting in significantly higher SINR at each antenna. Computer simulations demonstrated that the advanced RDM-RSMJ scheme achieves substantial improvements in error performance and SE compared to other existing modulation schemes for RIS-APs. A low-complexity

detector was also proposed, significantly reducing complexity while maintaining performance comparable to maximum likelihood detection. Furthermore, we derived a closed-form expression for the ABEP of RDM-RSM schemes by adapting a novel approach that models the conditional RIS reflection phases with a von Mises distribution. This analytical framework facilitated tractable error analysis and provided valuable insights into the operation of RDM-RSMJ. This framework also enables future extension of our analysis to a multi-mode version of the proposed RDM-RSMJ. The accuracy of the analytically derived ABEP expressions was validated by simulation results. Finally, we highlight that the analysis of the proposed RDM-RSM schemes under discrete RIS phase resolutions and imperfect CSI remains an important avenue for practical research.

APPENDIX A
PROOF OF THEOREM 1

In this section, we evaluate the expected value and variance of $\Re(\tilde{y}_l)$ and $\Im(\tilde{y}_l)$ for the RDM-RSMJ scheme, where $\tilde{y}_l = y_l s_A^*$. Due to symmetry, the following results also hold for $\Re(\tilde{y}_m)$ and $\Im(\tilde{y}_m)$, where $\tilde{y}_m = y_m s_B^*$.

A. Derivation of $\mu_R = \mathbb{E}\{\Re(\tilde{y}_l)\}$ and $\mu_I = \mathbb{E}\{\Im(\tilde{y}_l)\}$

We begin by considering a single-element RIS. For the synthesized signal x_l, we can expand $\mathbb{E}\{x_l\} = \mathbb{E}\{h_l e^{j\theta_l} e^{j\psi}\}$ as:

$$\mathbb{E}\{x_l\} = \mathbb{E}_{(h_l,\theta_l)}\left\{h_l e^{j\theta_l} \mathbb{E}_{\psi|(h_l,\theta_l)}\{e^{j\psi}|(h_l,\theta_l)\}\right\} \tag{62}$$

where

$$\mathbb{E}_{\psi|(h_l,\theta_l)}\{e^{j\psi}|(h_l,\theta_l)\} = \int_\Gamma e^{j\psi} f(\psi|h_l,\theta_l)\, d\psi \tag{63}$$

is the conditional expectation of $e^{j\psi}$. Here, $f(\psi|h_l,\theta_l)$ represents the probability density function (pdf) of the phase ψ, conditioned on h_l and θ_l. In the following, we discuss that $(\psi|h_l,\theta_l)$ follows Tikhonov distribution [37], which is also known as von Mises distribution in directional statistics [38].

To determine the conditional distribution of ψ, we draw upon results from a similar problem studied extensively in two different contexts: 1. Analog phase-locked loops (PLLs): Tikhonov [37] showed that the phase error, locked in a PLL tracking a constant-frequency sinusoidal signal in the presence of AWGN follows a distribution that cannot be formulated using simple functions. An approximate formula was derived, which became known as the Thikonov distribution [37], [38], [39]. The phase error, defined as $(\psi - \varphi_0)$, represents the phase difference between the local signal with deterministic phase φ_0 and an incoming reference signal whose phase ψ is randomly distributed around φ_0 due to the presence of AWGN, as illustrated in [39]. Since φ_0 is non-random (deterministic), the distribution of ψ is entirely determined by that of the phase error. 2. Phase noise problem: A similar problem has been widely studied in the context of phase noise, where the phase of a vector/sinusoid is perturbed by the addition of an AWGN signal. Studies have shown that the resulting phase noise can be approximated to follow the Tikhonov distribution [40], [41].

To leverage the results from the aforementioned literature, we model conditional ψ as the phase of a vector/sinusoid perturbed by AWGN, following the approach in [40] and [41]. Since $\psi = \angle S$, with $S = e^{j\phi_A} h_l e^{-j\theta_l} + e^{j\phi_B} h_m e^{-j\theta_m}$ (22). For given h_l and θ_l, the first component of S i.e., $e^{j\phi_A} h_l e^{-j\theta_l}$, can be modeled as a vector (RV) $a e^{j\varphi_0}$ with an amplitude $a = h_l$ and angle $\varphi_0 = \phi_A - \theta_l$. The second component, $e^{j\phi_B} h_m e^{-j\theta_m}$, is a CSCG RV following $\mathcal{CN}(0, 2\sigma_m^2)$. This component can be regarded as an AWGN signal with power $2\sigma_m^2$, which perturbs the phase of S around φ_0. Under these conditions, it is evident that $|S|$ follows Rician distribution [42], while the conditional ψ is approximated to have the following closed-form distribution function [39], [40], [41], [43]:

$$f(\psi|\kappa,\varphi_0) = \frac{\exp(\kappa\cos(\psi-\varphi_0))}{2\pi I_0(\kappa)}, \quad -\pi \le \psi \le \pi \tag{64}$$

In this equation, $\kappa(\gamma)$ is the shaping parameter that depends on the SNR $\gamma = h_l^2/2\sigma_m^2$ of the signal. For higher SNR values, $\kappa = \gamma$, provides a good approximation of the distribution [37], [39], [40]. In [44], $\kappa = \gamma(1 + be^{-c\gamma})$ is shown to provide a better approximation for a broader SNR range, where $b = 0.525$ and $c = 1.1503$. For the channel model considered in this study $\sigma_m^2 = 0.5$, hence the SNR $\gamma = h_l^2/2(0.5) = h_l^2$ for a given h_l. We can also write $\kappa(\gamma)$ as $\kappa(h_l)$.

Using the conditional pdf of ψ (64), and knowing that κ and φ_0 are functions of h_l and θ_l respectively, we can rewrite the expectation expression (63) as follows:

$$\begin{aligned}\mathbb{E}_{\psi|(h_l,\theta_l)}\{e^{j\psi}|(h_l,\theta_l)\} &= \int_{-\pi}^{\pi} e^{j\psi} f(\psi|\kappa,\varphi_0)\, d\psi \\ &= \int_{-\pi}^{\pi} e^{j\psi} \frac{e^{\kappa\cos(\psi+\theta_l-\phi_A)}}{2\pi I_0(\kappa)}\, d\psi. \end{aligned} \tag{65}$$

Notably, this is the first-order circular moment of the von Mises RV. The n^{th} order moment is given as:

$$\int_{-\pi}^{\pi} (e^{j\psi})^n f(\psi|\kappa,\varphi_0)\, d\psi = \frac{I_{|n|}(\kappa(h_l))}{I_0(\kappa(h_l))} e^{jn\varphi_0}, \tag{66}$$

where $I_n(\cdot)$ represents the modified Bessel function of the first kind of order n. The expression in (65) simplifies to the following by substituting (66) with $n = 1$:

$$\mathbb{E}_{\psi|(h_l,\theta_l)}\{e^{j\psi}|(h_l,\theta_l)\} = \frac{I_1(\kappa(h_l))}{I_0(\kappa(h_l))} e^{j(\phi_A-\theta_l)}. \tag{67}$$

By utilizing the above result and performing the integration in polar coordinates, the expression for $\mathbb{E}\{x_l\}$ (62) reduces to:

$$\mathbb{E}\{x_l\} = 2e^{j\phi_A} \int_0^\infty h_l^3 e^{-h_l^2} \frac{I_1(h_l^2(1+be^{-ch_l^2}))}{I_0(h_l^2(1+be^{-ch_l^2}))}\, dh_l. \tag{68}$$

The algebraic manipulation above utilizes the fact that h_l is Rayleigh-distributed with a pdf of $\frac{h_l e^{-h_l^2}}{0.5}$, while θ_l is uniformly distributed with a pdf of $\frac{1}{2\pi}$. The integral is solved numerically, and to prevent computational errors, the upper

limit of infinity is approximated as 10^5. The mean value of the signal $\tilde{x}_l = e^{-j\phi_A} x_l$ is calculated as follows:[2]

$$\mathbb{E}\{\tilde{x}_l\} \approx 0.626 \approx \sqrt{\pi}/2\sqrt{2}. \tag{69}$$

It is important to emphasize that the mean value of the signal $\tilde{x}_l = h_l e^{j(\psi-(\phi_A-\theta_l))}$ is real. This corroborates the fact that the von Mises distribution is symmetric around the mean phase, $\varphi_0 = \phi_A - \theta_l$. Consequently, from (69), we get:

$$\mathbb{E}\{\Re(\tilde{x}_l)\}=\Re(\mathbb{E}\{\tilde{x}_l\})=\sqrt{\pi}/2\sqrt{2}, \quad \mathbb{E}\{\Im(\tilde{x}_l)\}=\Im(\mathbb{E}\{\tilde{x}_l\})=0.$$

Now, incorporating the signal energy E and considering an RIS with N elements, the mean values of the real and imaginary parts of $\tilde{y}_l = s_A^* y_l$ where $y_l = \sqrt{E}\sum_{i=1}^{N} x_{l,i} + n_l$ can be expressed as:

$$\mu_R = \mathbb{E}\{\Re(\tilde{y}_l)\} = \frac{N\sqrt{\pi E}}{2\sqrt{2}}, \qquad \mu_I = \mathbb{E}\{\Im(\tilde{y}_l)\} = 0. \tag{70}$$

B. Evaluation of $\mathbb{V}\{\Re(\tilde{y}_l)\}$ and $\mathbb{V}\{\Im(\tilde{y}_l)\}$

We begin by considering the single-element RIS and compute the variance of the real part of the signal $\tilde{x}_l$ as follows:

$$\begin{aligned}\mathbb{V}\{\Re(\tilde{x}_l)\}&=\mathbb{E}\{(\Re(\tilde{x}_l))^2\}-(\mathbb{E}\{\Re(\tilde{x}_l)\})^2=\mathbb{E}\left\{\left(\frac{\tilde{x}_l+\tilde{x}_l^*}{2}\right)^2\right\}-\frac{\pi}{8}\\&=\frac{1}{4}\Big(\mathbb{E}\{\tilde{x}_l^2\}+\mathbb{E}\{\tilde{x}_l^{*2}\}+\mathbb{E}\{2h_l^2\}\Big)-\frac{\pi}{8}\end{aligned} \tag{71}$$

In the above, we utilized $\Re(\tilde{x}_l) = (\tilde{x}_l + \tilde{x}_l^*)/2$, $\tilde{x}_l\tilde{x}_l^* = h_l^2$, and we expanded the squares accordingly. To compute $\mathbb{E}\{\tilde{x}_l^2\}$, we follow the same steps used to evaluate $\mathbb{E}\{\tilde{x}_l\}$ earlier. Recognizing that $n = 2$ for the central moment expression (66) in this case, we derive:

$$\mathbb{E}\{\tilde{x}_l^2\}=\mathbb{E}\{e^{j2(\theta_l-\phi_A)}h_l^2 e^{j2\psi}\}=2\int_0^\infty h_l^4 e^{-h_l^2}\frac{I_2(\kappa(h_l))}{I_0(\kappa(h_l))}dh_l \tag{72}$$

Notably, $\mathbb{E}\{\tilde{x}_l^{*2}\}$ yields exactly the same expression as that for $\mathbb{E}\{\tilde{x}_l^2\}$ given above, resulting in $\mathbb{E}\{\tilde{x}_l^{*2}\} = \mathbb{E}\{\tilde{x}_l^2\}$. Moreover, $2h_l^2$ is central chi-squared RV with 2 degrees of freedom, leading to $\mathbb{E}\{2h_l^2\} = 2$ in our model. Therefore, we can consolidate these results into the variance calculation (71) as:[2]

$$\begin{aligned}\mathbb{V}\{\Re(\tilde{x}_l)\} &= \frac{1}{2}\mathbb{E}\{\tilde{x}_l^2\} + \frac{1}{2} - \frac{\pi}{8}\\ &= \int_0^\infty h_l^4 e^{-h_l^2}\frac{I_2(\kappa(h_l))}{I_0(\kappa(h_l))}\,dh_l + \frac{4-\pi}{8} \approx 0.355 \approx \frac{6-\pi}{8}\end{aligned} \tag{73}$$

[2]The mean value in (69) and the variance in (73) were obtained through numerical integration and subsequently approximated using closed-form representations involving π. These approximations have been verified to closely match the numerical results, with accuracy up to five decimal places. Related distribution problems have also been studied in [8], [10], and [25], where closed-form solutions involving π are derived using rectangular coordinate formulations—an approach particularly suitable for their proposed quadrature modulation schemes. These studies served as methodological references that guided and validated the final expressions involving π in our analysis. In this work, we instead adopt a polar coordinate formulation employing the von Mises distribution, which provides clearer geometric intuition for the design of the proposed RDM-RSM scheme and renders its error analysis more tractable. Moreover, this framework naturally extends the concept of RDM-RSM to its potential multi-mode version. Therefore, it is important to note that Eqs. (69) and (73) should be interpreted as accurate closed-form approximations rather than exact analytical results.

Next, we compute the variance of the imaginary part of $\tilde{x}_l$ as:

$$\begin{aligned}\mathbb{V}\{\Im(\tilde{x}_l)\}&=\mathbb{E}\{(\Im(\tilde{x}_l))^2\}-(\mathbb{E}\{\Im(\tilde{x}_l)\})^2=\mathbb{E}\left\{\left(\frac{\tilde{x}_l-\tilde{x}_l^*}{j2}\right)^2\right\}-0\\&=-\frac{1}{4}\mathbb{E}\Big\{\tilde{x}_l^2+\tilde{x}_l^{*2}-2\tilde{x}_l\tilde{x}_l^*\Big\}=-\left(\frac{1}{2}\mathbb{E}\{\tilde{x}_l^2\}-\frac{1}{2}\right)\\&=-(\mathbb{V}\{\Re(\tilde{x}_l)\}-1+\pi/8)=1/4\end{aligned} \tag{74}$$

In the algebraic manipulation above, we utilized $\Im(\tilde{x}_l) = \frac{\tilde{x}_l-\tilde{x}_l^*}{j2}$, $\mathbb{E}\{2\tilde{x}_l\tilde{x}_l^*\} = \mathbb{E}\{2h_l^2\} = 2$, and $\mathbb{E}\{\tilde{x}_l^2\}$ from (72).

Now, incorporating the signal energy E and considering an RIS with N elements, the variances of the real and imaginary parts of $\tilde{y}_l = s_A^* y_l$ where $y_l = \sqrt{E}\sum_{i=1}^{N} h_{l,i}e^{j\theta_{l,i}}e^{j\psi_i} + n_l$ can be expressed as follows:

$$\sigma_R^2 = \mathbb{V}\{\Re(\tilde{y}_l)\} = N(6-\pi)E/8 + N_0/2 \tag{75}$$

$$\sigma_I^2 = \mathbb{V}\{\Im(\tilde{y}_l)\} = NE/4 + N_0/2 \tag{76}$$

Moreover, the real and imaginary components of $\tilde{y}_l$ follow a Gaussian distribution under the assumption of CLT for large N (i.e., $N \gg 1$). These distributions can be expressed using the above-calculated means and variances as follows:

$$\Re(\tilde{y}_l)=\Re(y_l s_A^*) \sim \mathcal{N}\left(\frac{N\sqrt{\pi E}}{2\sqrt{2}}, \frac{N(6-\pi)E}{8}+\frac{N_0}{2}\right) \tag{77}$$

$$\Im(\tilde{y}_l) = \Im(y_l s_A^*) \sim \mathcal{N}\left(0, \frac{NE}{4}+\frac{N_0}{2}\right) \tag{78}$$

The expressions in (77) and (78) correspond to the general case with signal energy E. For $E = 1$, a setting adopted for analytical convenience in the section where Theorem 1 is presented, these expressions simplify to the following form:

$$\Re(\tilde{y}_l)=\Re(y_l s_A^*) \sim \mathcal{N}\left(\frac{N\sqrt{\pi}}{2\sqrt{2}}, \frac{N(6-\pi)}{8}+\frac{N_0}{2}\right) \tag{79}$$

$$\Im(\tilde{y}_l) = \Im(y_l s_A^*) \sim \mathcal{N}\left(0, \frac{N}{4}+\frac{N_0}{2}\right). \tag{80}$$

This concludes the proof of Theorem 1.

Appendix B
Derivation of $\sigma_{R,I} = \mathbb{C}\{\Re(\tilde{y}_l), \Im(\tilde{y}_l)\}$

We begin with the single-element RIS, and first compute the covariance between the real and imaginary parts of $\tilde{x}_l$:

$$\begin{aligned}\mathbb{C}\{\Re(\tilde{x}_l),\Im(\tilde{x}_l)\}&=\mathbb{E}\{\Re(\tilde{x}_l)\Im(\tilde{x}_l)\}-\mathbb{E}\{\Re(\tilde{x}_l)\}\mathbb{E}\{\Im(\tilde{x}_l)\}\\&=\mathbb{E}\left\{\left(\frac{\tilde{x}_l+\tilde{x}_l^*}{2}\right)\left(\frac{\tilde{x}_l-\tilde{x}_l^*}{j2}\right)\right\}-\frac{\sqrt{\pi}}{2\sqrt{2}}\cdot 0=0\end{aligned} \tag{81}$$

Thus, the real and imaginary parts of the synthesized signal $\tilde{x}_l$ are uncorrelated for a single-element RIS. For an RIS with N elements, the pairs $\{\Re(\tilde{x}_{l,i}), \Im(\tilde{x}_{l,i})\}$ are i.i.d. Therefore, $\mathbb{C}\{\Re(\tilde{x}_{l,i}), \Im(\tilde{x}_{l,j})\} = 0$ for $i \neq j$, and it is also equal to 0 when $i = j$ as computed above (81). Thus, we have:

$$\mathbb{C}\Big\{\Re(\tilde{x}_l), \Im(\tilde{x}_l)\Big\} = \mathbb{C}\left\{\sum_{i=1}^{N}\Re(\tilde{x}_{l,i}), \sum_{j=1}^{N}\Im(\tilde{x}_{l,j})\right\}$$

$$=\sum_{i=1}^{N}\sum_{j=1}^{N}\mathbb{C}\{\Re(\tilde{x}_{l,i}), \Im(\tilde{x}_{l,j})\}=\sum_{i=1}^{N}\mathbb{C}\{\Re(\tilde{x}_{l,i}),\Im(\tilde{x}_{l,i})\}=0$$

Since $\Re(x_l) = \sum_{i=1}^{N} \Re(\tilde{x}_{l,i})$ and $\Im(x_l) = \sum_{i=1}^{N} \Im(\tilde{x}_{l,i})$ are approximated as Gaussian under the CLT for an RIS with $N \gg 1$, their uncorrelatedness implies independence. Moreover, the orthogonal components of n_l are independent, which leads to:

$$\sigma_{R,I} = \mathbb{C}\{\Re(\tilde{y}_l), \Im(\tilde{y}_l)\} = 0. \tag{82}$$

APPENDIX C
DERIVATION OF $\sigma_{R,R} = \mathbb{C}\{\Re(\tilde{y}_l), \Re(\tilde{y}_m)\}$

We first calculate the covariance between $\Re(\tilde{x}_l)$ and $\Re(\tilde{x}_m)$ for a single-element RIS using the following approach:

$$\mathbb{V}\{\Re(\tilde{x}_l) + \Re(\tilde{x}_m)\} = \mathbb{V}\left\{\frac{\tilde{x}_l + \tilde{x}_l^*}{2} + \frac{\tilde{x}_m + \tilde{x}_m^*}{2}\right\}$$
$$= \frac{1}{2}\mathbb{V}\left\{(\tilde{x}_l + \tilde{x}_m) + (\tilde{x}_l + \tilde{x}_m)^*\right\} = \mathbb{V}\{|S|\} = \frac{4-\pi}{2}. \tag{83}$$

The above simplification uses the fact that $\tilde{x}_l + \tilde{x}_m = e^{-j\phi_A} h_l e^{j\theta_l} e^{j\psi} + e^{-j\phi_B} h_m e^{j\theta_m} e^{j\psi} = |S|$ in accordance with (21), and $|S|$ is Rayleigh-distributed with variance $(4-\pi)/2$.

Alternatively,

$$\mathbb{V}\{\Re(\tilde{x}_l) + \Re(\tilde{x}_m)\} = \mathbb{V}\{\Re(\tilde{x}_l)\} + \mathbb{V}\{\Re(\tilde{x}_m)\} + 2\mathbb{C}\{\Re(\tilde{x}_l), \Re(\tilde{x}_m)\}$$
$$= 2\mathbb{V}\{\Re(\tilde{x}_l)\} + 2\mathbb{C}\{\Re(\tilde{x}_l), \Re(\tilde{x}_m)\} = 2\left(\frac{6-\pi}{8} + \mathbb{C}\{\Re(\tilde{x}_l), \Re(\tilde{x}_m)\}\right)$$

Substituting $\mathbb{V}\{\Re(\tilde{x}_l) + \Re(\tilde{x}_m)\}$ in the above from (83), we get:

$$\mathbb{C}\{\Re(\tilde{x}_l), \Re(\tilde{x}_m)\} = (2-\pi)/8. \tag{84}$$

For an RIS with N elements and signal energy as E, we have:

$$\mathbb{C}\left\{\Re(\tilde{x}_l), \Re(\tilde{x}_m)\right\} = \mathbb{C}\left\{\sum_{i=1}^{N} \Re(\tilde{x}_{l,i}), \sum_{j=1}^{N} \Re(\tilde{x}_{m,j})\right\}$$

$$= \sum_{i=1}^{N} \mathbb{C}\{\Re(\tilde{x}_{l,i}), \Re(\tilde{x}_{m,i})\} = N(2-\pi)E/8. \tag{85}$$

Finally, the uncorrelated noise at both antennas leads to:

$$\sigma_{R,R} = \mathbb{C}\left\{\Re(\tilde{y}_l), \Re(\tilde{y}_m)\right\} = N(2-\pi)E/8. \tag{86}$$

APPENDIX D
DDERIVATION OF $\sigma_{I,I} = \mathbb{C}\{\Im(\tilde{y}_l), \Im(\tilde{y}_m)\}$

We first calculate the covariance between $\Im(\tilde{x}_l)$ and $\Im(\tilde{x}_m)$ for a single-element RIS using the following approach:

$$\mathbb{V}\{\Im(\tilde{x}_l) + \Im(\tilde{x}_m)\} = \mathbb{V}\left\{\frac{\tilde{x}_l - \tilde{x}_l^*}{2j} + \frac{\tilde{x}_m - \tilde{x}_m^*}{2j}\right\}$$
$$= \mathbb{V}\left\{\frac{\tilde{x}_l + \tilde{x}_m}{2j} - \frac{(\tilde{x}_l + \tilde{x}_m)^*}{2j}\right\} = \frac{1}{j2}\mathbb{V}\{|S| - |S|\} = 0. \tag{87}$$

Alternatively,

$$\mathbb{V}\{\Im(\tilde{x}_l) + \Im(\tilde{x}_m)\} = \mathbb{V}\{\Im(\tilde{x}_l)\} + \mathbb{V}\{\Im(\tilde{x}_m)\} + 2\mathbb{C}\{\Im(\tilde{x}_l), \Im(\tilde{x}_m)\}$$
$$= 2\left(1/4 + \mathbb{C}\{\Im(\tilde{x}_l), \Im(\tilde{x}_m)\}\right) \tag{88}$$

Substituting $\mathbb{V}\{\Im(\tilde{x}_l) + \Im(\tilde{x}_m)\}$ in the above from (87), we get:

$$\mathbb{C}\{\Im(\tilde{x}_l), \Im(\tilde{x}_m)\} = -1/4 \tag{89}$$

It implies the correlation coefficient is equal to -1. For an RIS with N elements and energy of the signal as E, we have:

$$\mathbb{C}\left\{\Im(\tilde{x}_l), \Im(\tilde{x}_m)\right\} = \mathbb{C}\left\{\sum_{i=1}^{N} \Im(\tilde{x}_{l,i}), \sum_{j=1}^{N} \Im(\tilde{x}_{m,j})\right\}$$

$$= \sum_{i=1}^{N} \mathbb{C}\{\Im(\tilde{x}_{l,i}), \Im(\tilde{x}_{m,i})\} = -NE/4. \tag{90}$$

Consequently, due to independence of noise, we get:

$$\sigma_{I,I} = \mathbb{C}\left\{\Im(\tilde{y}_l), \Im(\tilde{y}_m)\right\} = -NE/4. \tag{91}$$

APPENDIX E
EDERIVATION OF SIGNAL STATISTICS FOR RDM-RSMI

Here we derive the received signal statistics for RDM-RSMI scheme, for an RIS with N elements and signal energy E. The results from (15) and (16), directly leads to the following:

$$\mu_R = \mathbb{E}\{\Re(\tilde{y}_l)\} = N\sqrt{\pi E}/4, \quad \mu_I = \mathbb{E}\{\Im(\tilde{y}_l)\} = 0 \tag{92}$$

$$\sigma_R^2 = \mathbb{V}\{\Re(\tilde{y}_l)\} = N(6-\pi)E/8 + N_0/2 \tag{93}$$
$$\sigma_I^2 = \mathbb{V}\{\Im(\tilde{y}_l)\} = NE/4 + N_0/2 \tag{94}$$

Since the signals on both correct antennas are uncorrelated, the following covariances are zero:

$$\sigma_{R,R} = \mathbb{C}\left\{\Re(\tilde{y}_l), \Re(\tilde{y}_m)\right\} = 0, \tag{95}$$
$$\sigma_{I,I} = \mathbb{C}\left\{\Im(\tilde{y}_l), \Im(\tilde{y}_m)\right\} = 0 \tag{96}$$

The fact that RVs A_l and B_l in the expression for $\tilde{y}_l$ (follows from (8)) are independent (as they result from two independently configured RIS partitions) and that RV B_l is CSCG directly leads to:

$$\sigma_{R,I} = \mathbb{C}\{\Re(\tilde{y}_l), \Im(\tilde{y}_l)\} = 0, \tag{97}$$

REFERENCES

[1] E. Basar, M. Wen, R. Mesleh, M. Di Renzo, Y. Xiao, and H. Haas, "Index modulation techniques for next-generation wireless networks," *IEEE Access*, vol. 5, pp. 16693–16746, 2017.

[2] M. Wen et al., "A survey on spatial modulation in emerging wireless systems: Research progresses and applications," *IEEE J. Sel. Areas Commun.*, vol. 37, no. 9, pp. 1949–1972, Sep. 2019.

[3] J. Wang, S. Jia, and J. Song, "Generalised spatial modulation system with multiple active transmit antennas and low complexity detection scheme," *IEEE Trans. Wireless Commun.*, vol. 11, no. 4, pp. 1605–1615, Apr. 2012. [Online]. Available: https://api.semanticscholar.org/CorpusID:7219282

[4] E. Basar, M. Di Renzo, J. De Rosny, M. Debbah, M.-S. Alouini, and R. Zhang, "Wireless communications through reconfigurable intelligent surfaces," *IEEE Access*, vol. 7, pp. 116753–116773, 2019.

[5] W. Yan, X. Yuan, Z.-Q. He, and X. Kuai, "Passive beamforming and information transfer design for reconfigurable intelligent surfaces aided multiuser MIMO systems," *IEEE J. Sel. Areas Commun.*, vol. 38, no. 8, pp. 1793–1808, Aug. 2020.

[6] S. Lin, B. Zheng, G. C. Alexandropoulos, M. Wen, M. D. Renzo, and F. Chen, "Reconfigurable intelligent surfaces with reflection pattern modulation: Beamforming design and performance analysis," *IEEE Trans. Wireless Commun.*, vol. 20, no. 2, pp. 741–754, Feb. 2021.

[7] T. Ahmad and E. Basar, "Efficient indexing schemes for quadrature reflection modulation in RIS-based BackCom," *IEEE Trans. Commun.*, vol. 72, no. 9, pp. 5781–5795, Sep. 2024.

[8] M. H. Dinan, M. D. Renzo, and M. F. Flanagan, "RIS-assisted receive quadrature spatial modulation with low-complexity greedy detection," *IEEE Trans. Commun.*, vol. 71, no. 11, pp. 6546–6560, Nov. 2023.

[9] E. Basar, "Reconfigurable intelligent surface-based index modulation: A new beyond MIMO paradigm for 6G," *IEEE Trans. Commun.*, vol. 68, no. 5, pp. 3187–3196, May 2020.

[10] J. Yuan, M. Wen, Q. Li, E. Basar, G. C. Alexandropoulos, and G. Chen, "Receive quadrature reflecting modulation for RIS-empowered wireless communications," *IEEE Trans. Veh. Technol.*, vol. 70, no. 5, pp. 5121–5125, May 2021.

[11] X. Cai, C. Huang, P. Chen, E. Basar, and C. Yuen, "Design of non-coherent RIS-empowered DCSK with two-level nested index modulation," *IEEE Trans. Wireless Commun.*, vol. 24, no. 4, pp. 3044–3058, Apr. 2025.

[12] Z. Wan et al., "RIS-assisted integration of communications and security: Protocol, prototyping, and field trials," *IEEE Internet Things J.*, vol. 11, no. 16, pp. 26877–26887, Aug. 2024.

[13] S. Zeng, H. Zhang, B. Di, Z. Han, and L. Song, "Reconfigurable intelligent surface (RIS) assisted wireless coverage extension: RIS orientation and location optimization," *IEEE Commun. Lett.*, vol. 25, no. 1, pp. 269–273, Jan. 2021.

[14] X. Cai et al., "Toward RIS-aided non-coherent communications: A joint index keying M-ary differential chaos shift keying system," *IEEE Trans. Wireless Commun.*, vol. 22, no. 12, pp. 9045–9062, Dec. 2023.

[15] X. Cai, C. Yuen, C. Huang, W. Xu, and L. Wang, "Toward chaotic secure communications: An RIS enabled M-ary differential chaos shift keying system with block interleaving," *IEEE Trans. Commun.*, vol. 71, no. 6, pp. 3541–3558, Jun. 2023.

[16] W. Saad, M. Bennis, and M. Chen, "A vision of 6G wireless systems: Applications, trends, technologies, and open research problems," *IEEE Netw.*, vol. 34, no. 3, pp. 134–142, May 2020.

[17] D. C. Nguyen et al., "6G Internet of Things: A comprehensive survey," *IEEE Internet Things J.*, vol. 9, no. 1, pp. 359–383, Jan. 2022.

[18] M. Di Renzo et al., "Smart radio environments empowered by reconfigurable intelligent surfaces: How it works, state of research, and the road ahead," *IEEE J. Sel. Areas Commun.*, vol. 38, no. 11, pp. 2450–2525, Nov. 2020.

[19] Y. Chen, W. Cheng, and W. Zhang, "Reconfigurable intelligent surface equipped UAV in emergency wireless communications: A new fading–shadowing model and performance analysis," *IEEE Trans. Commun.*, vol. 72, no. 3, pp. 1821–1834, Mar. 2024.

[20] B. Ji et al., "Vehicular communication based on RIS-assisted source: RIS-relay versus energy harvesting relay," *IEEE Trans. Intell. Transp. Syst.*, vol. 26, no. 10, pp. 17442–17461, Oct. 2025.

[21] H. Wymeersch, J. He, B. Denis, A. Clemente, and M. Juntti, "Radio localization and mapping with reconfigurable intelligent surfaces: Challenges, opportunities, and research directions," *IEEE Veh. Technol. Mag.*, vol. 15, no. 4, pp. 52–61, Dec. 2020.

[22] M. I. Ismail, A. M. Shaheen, M. M. Fouda, and A. S. Alwakeel, "RIS-assisted integrated sensing and communication systems: Joint reflection and beamforming," *IEEE Open J. Commun.*, vol. 5, pp. 908–927, 2024.

[23] X. Yu, D. Xu, Y. Sun, D. W. K. Ng, and R. Schober, "Robust and secure wireless communications via intelligent reflecting surfaces," *IEEE J. Sel. Areas Commun.*, vol. 38, no. 11, pp. 2637–2652, Nov. 2020.

[24] R. Kaur, B. Bansal, S. Majhi, S. Jain, C. Huang, and C. Yuen, "A survey on reconfigurable intelligent surface for physical layer security of next-generation wireless communications," *IEEE Open J. Veh. Technol.*, vol. 5, pp. 172–199, 2024.

[25] M. H. Dinan, N. S. Perovic, and M. F. Flanagan, "RIS-assisted receive quadrature space-shift keying: A new paradigm and performance analysis," *IEEE Trans. Commun.*, vol. 70, no. 10, pp. 6874–6889, Oct. 2022.

[26] M. H. Dinan and M. F. Flanagan, "RIS-assisted generalized receive quadrature spatial modulation," in *Proc. GLOBECOM IEEE Global Commun. Conf.*, Dec. 2023, pp. 2876–2881.

[27] L. Zhang, X. Lei, Y. Xiao, and T. Ma, "Large intelligent surface-based generalized index modulation," *IEEE Commun. Lett.*, vol. 25, no. 12, pp. 3965–3969, Dec. 2021.

[28] M. Wen, E. Basar, Q. Li, B. Zheng, and M. Zhang, "Multiple-mode orthogonal frequency division multiplexing with index modulation," *IEEE Trans. Commun.*, vol. 65, no. 9, pp. 3892–3906, Sep. 2017.

[29] E. Yoon, S.-Y. Kim, S. Kwon, and U. Yun, "An efficient index mapping algorithm for OFDM-index modulation," *IEEE Access*, vol. 7, pp. 184194–184206, 2019.

[30] Y. Bian, X. Cheng, M. Wen, L. Yang, H. V. Poor, and B. Jiao, "Differential spatial modulation," *IEEE Trans. Veh. Technol.*, vol. 64, no. 7, pp. 3262–3268, Jul. 2015.

[31] Q. Wu and R. Zhang, "Intelligent reflecting surface enhanced wireless network via joint active and passive beamforming," *IEEE Trans. Wireless Commun.*, vol. 18, no. 11, pp. 5394–5409, Nov. 2019.

[32] E. Björnson and L. Sanguinetti, "Rayleigh fading modeling and channel hardening for reconfigurable intelligent surfaces," *IEEE Wireless Commun. Lett.*, vol. 10, no. 4, pp. 830–834, Apr. 2021.

[33] M. Di Renzo and H. Haas, "Bit error probability of SM-MIMO over generalized fading channels," *IEEE Trans. Veh. Technol.*, vol. 61, no. 3, pp. 1124–1144, Mar. 2012.

[34] J. G. Proakis, *Digital Communications*, 5th ed. New York, NY, USA: McGraw-Hill, 2008.

[35] M. Simon and M. S. Alouini, *Digital Communications Over Fading Channels*, 2nd ed., Hoboken, NJ, USA: Wiley, 2005.

[36] E. Basar, "Transmission through large intelligent surfaces: A new frontier in wireless communications," in *Proc. Eur. Conf. Netw. Commun. (EuCNC)*, Jun. 2019, pp. 112–117.

[37] V. I. Tikhonov, "The effect of noise on phase-lock oscillation operation," *Automatika Telemekhan.*, vol. 20, no. 9, pp. 1188–1196, Sep. 1959.

[38] D. J. Best and N. I. Fisher, "The BIAS of the maximum likelihood estimators of the von mises-Fisher concentration parameters," *Commun. Statist. Simul. Comput.*, vol. 10, no. 5, pp. 493–502, Jan. 1981.

[39] A. J. Viterbi, "Phase-locked loop dynamics in the presence of noise by Fokker-Planck techniques," *Proc. IEEE*, vol. 51, no. 12, pp. 1737–1753, Dec. 1963.

[40] H. Leib and S. Pasupathy, "The phase of a vector perturbed by Gaussian noise and differentially coherent receivers," *IEEE Trans. Inf. Theory*, vol. 34, no. 6, pp. 1491–1501, Nov. 1988.

[41] H. Fu and P. Yuen Kam, "Exact phase noise model and its application to linear minimum variance estimation of frequency and phase of a noisy sinusoid," in *Proc. IEEE 19th Int. Symp. Pers., Indoor Mobile Radio Commun.*, Cannes, France, Sep. 2008, pp. 1–5.

[42] S. O. Rice, "Statistical properties of a sine wave plus random noise," *Bell Syst. Tech. J.*, vol. 27, no. 1, pp. 109–157, Jan. 1948.

[43] Y. S. Shmaliy, "Probability density of the phase of a random RF pulse in the presence of Gaussian noise," *AEU Int. J. Electron. Commun.*, vol. 63, no. 1, pp. 15–23, Jan. 2009.

[44] Y. S. Shmaliy, "Von Mises/Tikhonov-based distributions for systems with differential phase measurement," *Signal Process.*, vol. 85, no. 4, pp. 693–703, Apr. 2005.